Mylpf dosage is proportionate to fast-twitch myofibril size in the zebrafish embryo

Authors:
Tayo E Adekeye – School of Biology and Ecology, the University of Maine, 04469, USA
Emily M Teets – Molecular Genetics, The Ohio State University, 43210, USA
Emily A Tomak – School of Biology and Ecology, the University of Maine, 04469, USA
Sadie L Waterman – School of Biology and Ecology, the University of Maine, 04469, USA
Kailee A Sprague – School of Biology and Ecology, the University of Maine, 04469, USA
Angelina White – School of Biology and Ecology, the University of Maine, 04469, USA
Maddison L Coffin – School of Biology and Ecology, the University of Maine, 04469, USA
Sabrina M Varga – School of Biology and Ecology, the University of Maine, 04469, USA
Teresa E Easterbrooks – School of Biology and Ecology, the University of Maine, 04469, USA
Sarah J Shepherd – Molecular Genetics, The Ohio State University, 43210, USA
Jared D Austin – School of Biology and Ecology, the University of Maine, 04469, USA
Dmitrii Krivorotko – School of Biology and Ecology, the University of Maine, 04469, USA
Troy E Hupper – School of Biology and Ecology, the University of Maine, 04469, USA
Joshua B Kelley – Molecular and Biomedical Sciences, the University of Maine, 04469, USA
Sharon L Amacher – Departments of Molecular Genetics and Biological Chemistry and Pharmacology, The Ohio State University, 43210, USA
* Jared C Talbot – School of Biology and Ecology, the University of Maine, 04469, USA

* Corresponding author
Phone: 207-581-2835
Email: jared.talbot@maine.edu

Abstract

Muscle cells become stronger by expanding myofibrils, the chains of sarcomeres that produce contraction. Here we investigate how Mylpf (Myosin Light Chain Phosphorylatable Fast) abundance impacts myofibril assembly in fast-twitch muscle. The two zebrafish Mylpf genes (*mylpfa* and *mylpfb*) are exclusively expressed in fast-twitch muscle. We show that these cells initially produce six times more *mylpfa* mRNA and protein than *mylpfb*. The combined Mylpf protein dosage is necessary for and proportionate to fast-twitch myofibril growth in the embryo. Fast-twitch myofibrils are severely reduced in the *mylpfa*$^{-/-}$ mutant, leading to loss of high-speed movement; however, by persistent slow movement this mutant swims as far through time as its wild-type sibling. Although the *mylpfb*$^{-/-}$ mutant has normal myofibrils, myofibril formation fails entirely in the *mylpfa*$^{-/-}$;*mylpfb*$^{-/-}$ double mutant, indicating that the two genes are collectively essential to myofibril formation. Fast-twitch myofibril width is restored in the *mylpfa*$^{-/-}$ mutant by transgenic expression of *mylpfa-GFP, mylpfb-GFP,* and by human *MYLPF-GFP* to a degree corresponding linearly with GFP brightness. This correlate is inverted by expression of *MYLPF* alleles that cause Distal Arthrogryposis, which reduce myofibril size in proportion to protein abundance. These effects indicate that Mylpf dosage controls myofibril growth, impacting embryonic development and lifelong health.

Introduction

The myofibril is the contractile organelle of striated muscle, made of chains of sarcomeres that span the cell's length (Figure 1A). Sarcomeres form on the scale of microns, yet their collective function in myofibrils can impact behavior of the entire organism. Despite the importance of myofibril structure and size to muscle strength, it remains unclear how myofibril growth is regulated. One way to control myofibril growth is to regulate the abundance of its component parts. Protein levels ('dosage') are influenced by many factors including a gene's copy number, the amount of steady-state transcript produced by each gene ('mRNA abundance'), the steady-state amount of protein encoded by these genes ('protein abundance'), the activity of each encoded protein, and the protein's localization within a cell. In this study, we investigate how the abundance of one key sarcomeric component, Mylpf, impacts myofibril formation. We find that overall Mylpf dosage is controlled by a combination of gene copy number and mRNA abundance, which together predict protein abundance and myofibril size in the zebrafish embryo.

Initially, myofibril formation growth is directed by actin-rich thin filaments [1–3]. These thin filaments contain F-actin strands bundled with nebulin and linked to actinin-rich Z-disks, producing I-Z-I bodies. The ends of I-Z-I bodies are temporarily connected to one another by non-muscle myosin to form pre-myofibrils, which act as a template for further growth [3–7]. Growth is also facilitated in part by integration of enormous contractile proteins titin and nebulin, which set the sarcomere's length [8]. Once pre-myofibrils have formed, the non-muscle myosin is quickly replaced by contractile myosin heavy chain (MyHC), bundled into double-headed thick filaments. These added thick filaments increase tension across the muscle cell, leading to myofibrillar growth [9–11]. Myofibril size then increases along the muscle cell's narrow axis (the 'width axis'), beginning near the cell membrane and then extending into the central cytoplasm[11]. Growth along the width axis increases the myofibril's cross-sectional area, which predicts muscle strength better than overall muscle size does [14].

The class II MyHC in thick filaments is stabilized close to its force-generating head by a Regulatory Light Chain (RLC) and an Essential Light Chain (ELC) protein [12,13]. These light chains regulate myosin movement and force generation but do not consume ATP nor produce force on their own [12]. Point mutations in the RLCs can reduce myosin step size [14], and outright removal of these light chains *in vitro* causes MyHC aggregation and partially reduces MyHC activity [15,16]. Consistent with this finding, the *Drosophila* RLC mutant lacks skeletal muscle [17]. Similarly, the ELC gene *Myl1* is required for normal myogenesis in chicken, zebrafish, mouse, and human [18–20]. Because the primary effect of these light chains is to regulate and stabilize MyHC, we hypothesize that myosin light chain proteins influence the rate of cytoskeletal organization leading to myofibril growth, independent of cell size regulation.

Mylpf (Myosin Light Chain Phosphorylatable Fast) is a light chain of particular interest because it is the only RLC with prominent expression in embryonic muscle fibers and differentiated fast-twitch skeletal muscle in the mouse [21]. All skeletal muscle fibers are absent from the mouse *Mylpf* knockout at birth, suggesting that in mouse this gene may be required in all embryonic fibers [22]. Muscle loss in the *Mylpf*$^{-/-}$ mutant is so complete that it is unclear what phase of myogenesis is disrupted by the mutation. *MYLPF* function is also critical for human development. Missense alleles in *MYLPF* cause Distal Arthrogryposis (DA), a congenital musculoskeletal disease characterized by inherited distal limb contractures [23]. DA is often caused by mutation in genes that encode contractile proteins [24,25]. However, muscle strength nor structure was not examined in human patients with the MYLPF variants, and the impact of those variants have not been tested in animal models. Therefore, the impact of *MYLPF* missense alleles on muscle remains unresolved.

In vertebrates, muscle formation begins in segments of mesoderm called somites, which eventually produce most of the muscles in the body. Somite development proceeds quickly in zebrafish, leading to formation of two fiber types, fast-twitch and slow-twitch, within the first day post fertilization (dpf) [26]. Whereas slow-twitch fibers

106 contract and fatigue slowly, the zebrafish fast-twitch fibers contract with such speed and
107 power that they nearly strain muscle cells to the point of snapping [27,28]. In zebrafish, the
108 slow-twitch fibers are specified in the medial edge of the somite, then most of these
109 cells migrate to the lateral surface of the somite adjacent to the ectoderm, leaving
110 behind only a set medial slow muscle at the horizontal myoseptum [26]. By 24 hours post
111 fertilization (hpf), all muscle fibers medial to this thin slow-twitch layer are fast-twitch [26].
112 These positions are retained through embryonic development, enabling us to identify
113 fiber types by position in addition to molecular markers of fiber type. Muscle fibers grow
114 continuously during embryonic development, more than doubling in size by the time of
115 hatching (3 dpf) [29]. Hatched larvae continue growing while subsisting on their yolk until 6
116 dpf, enabling study of early larval growth independent of feeding.
117
118 In zebrafish, Mylpf gene function is distributed across two paralogs, *mylpfa* and *mylpfb*
119 [30–33]. Each gene has one primary transcript in the University of California Santa Cruz
120 genome browser and in Ensembl (Figure 1B) [34]. The two zebrafish Mylpf proteins are
121 94% identical to one another and each is 89% identical to human MYLPF in both
122 primary sequence and predicted protein structure (Figure 1C). The *mylpfa* and *mylpfb*
123 frameshifting alleles used in this study are predicted to be functionally null because they
124 truncate proteins within the first of two calcium-binding EF-Hand domains (Figure 1D).
125 We previously showed that zebrafish *mylpfa*$^{-/-}$ mutant animals can form multinucleate
126 muscle cells but have weakened muscle that eventually deteriorates [35]. However, the
127 impact of *mylpfa* on myofibrils remained untested and the requirements for *mylpfb*
128 function in embryonic development remained unexplored.
129
130 Here, we investigate the effect of Mylpf activity on myofibril development within the
131 somite. We generated a frameshifting *mylpfb* mutation within the first EF-Hand domain,
132 to mirror published [35] *mylpfa* alleles (Figure 1B-E). This *mylpfb*$^{-/-}$ mutant alone has no
133 overt muscle defect, but the *mylpfb* mutation enhances the *mylpfa*$^{-/-}$ mutant phenotype.
134 Examination of animals heterozygous or homozygous for the two mutations reveals that
135 myofibril widths in loss of function are predicted by wild-type Mylpf dosage. Transgenic
136 expression of *mylpfa* and *mylpfb* efficiently rescues the *mylpfa*$^{-/-}$ mutant when either

137 gene is expressed at high abundance. A transgene expressing human *MYLPF* also
138 rescues the mutant, suggesting conserved function across vertebrate taxa. By contrast,
139 expression of *MYLPF* alleles thought to cause DA ('DA-causing' alleles) disrupt myofibril
140 formation in the *mylpfa*$^{+/+}$ wild-type zebrafish, with a dominant human allele causing
141 more severe defects than a recessive human allele. Together, these findings suggest
142 that Mylpf activity controls myofibril growth by promoting MyHC localization to the site of
143 myofibril formation during early fast-twitch myogenesis.
144

145 # Results

146

147 ***mylpfa* mRNA and Mylpfa protein are expressed more abundantly than *mylpfb* /**
148 **Mylpfb during embryonic development**

149 Although *mylpfa* and *mylpfb* expression patterns have been described individually [36],
150 their overlap and relative abundance have not been clarified. Transcripts for both Mylpf
151 genes are restricted to fast-twitch muscle, but the *mylpfb* labeling is dimmer as
152 assessed by Hybridization Chain Reaction based RNA *in situ* hybridization (HCR ISH)
153 (Figure 1F-H, S1). Neither gene is expressed in slow-twitch muscle, which expresses a
154 different regulatory light chain, *myl10* (Figure 1F) [37]. Expression of *mylpfa* and *mylpfb* is
155 seen as early as 20 hpf in medial fast-twitch fibers (Figure S1). At 24 hpf, expression of
156 *mylpfa* is around 6 times greater than *mylpfb* when assessed by HCR ISH. The ratio
157 decreases to 3:1 by 36 hpf, largely because of rising *mylpfb* mRNA abundance (Figure
158 1G, H). Expression of *mylpfa* remains more abundant than *mylpfb* through embryonic
159 stages (Figure 1G, H). Our HCR ISH finding at 24 hpf is close to the 7 to 1 ratio we find
160 for *mylpfa* and *mylpfb* at 27 hpf in an RNA-seq dataset we previously published (Figure
161 1I) [38]. To investigate whether transcript levels predict protein abundance, we generated
162 and tested new antibodies that recognize both Mylpfa and Mylpfb, which we find to differ
163 by 2 kilodaltons (kD). The relative protein abundance correlates with transcript levels.
164 For instance, the Mylpfa and Mylpfb proteins are expressed in a 6:1 ratio at 24 hpf and
165 3:1 at 36 hpf (Figure 1I, J). We confirmed antibody specificity by examining the *mylpfa*$^{-/-}$
166 mutant embryos at 72 hpf. The mutant lacks the Mylpfa band without any change in the

167 Mylpfb band intensity (Figure 1K). In summary, the two zebrafish Mylpf genes are
168 expressed in fast-twitch muscle, but Mylpfa is produced more abundantly than Mylpfb.
169
170 ***mylpfa* is required for the localization of fast-twitch myofibril components, but not**
171 **for muscle size**
172 To investigate the possibility that the abundant gene *mylpfa* is required for myofibril
173 structure, we compared F-actin localization in the *mylpfa*$^{-/-}$ mutant to its wild-type sibling
174 at 48 hpf, when the fast-twitch myofibrils have thickened. The *mylpfa*$^{-/-}$ mutants have
175 normal slow-twitch fibers but severely disordered F-actin in fast-twitch muscle (Figure
176 2A-B', S2). Only a small amount of myofibril forms within the fast-twitch muscle of the
177 *mylpfa*$^{-/-}$ mutant (Figure 2C). This myofibril growth defect reflects a failure to organize
178 subcellular components of the myofibril, not overall muscle growth. For instance, the
179 somite's cross-sectional area is unchanged in the *mylpfa*$^{-/-}$ mutant (Figure 2A'', B'', D).
180 Likewise, western blot indicates that MyHC abundance is unchanged in the *mylpfa*$^{-/-}$
181 homozygotes, suggesting that there is ample protein production (Figure 2E-E'). Total
182 Mylpf abundance is reduced to 54% because Mylpfa protein is completely lost and there
183 is little compensation by Mylpfb (Figures 1L, 2E-E'). Other myofibril markers are also
184 expressed with wild-type abundance but show impaired organization in the *mylpfa*$^{-/-}$
185 mutant (Figure 2F-I). The myofibrils are narrower in the mutant, but sarcomere length is
186 unchanged (Figure 2J). Using this constant length, we developed an image analysis
187 protocol that assesses the fraction of protein in an image localized to sarcomere-length
188 objects, which we dub the 'sarcomeric fraction' (Figure S3). The sarcomeric-fraction is
189 reduced by half in the *mylpfa*$^{-/-}$ mutant fast-twitch muscle for all proteins tested,
190 matching the reduction in overall Mylpf protein abundance (Figure 2K-L, S3). We
191 generated a *mylpfa:mylpfa-GFP* Tol2 transgene, which produces Mylpfa-GFP protein at
192 around half the native level (Figure 3A, B). This transgene restores both the sarcomeric
193 fraction and myofibril width in the *mylpfa*$^{-/-}$ mutant (Figure 3C-F). This myofibril
194 restoration persists to at least 6 dpf, though some delocalized GFP is seen at that later
195 time-point (Figure 3G, S4). Together these findings show that *mylpfa* has no impact on
196 overall muscle size but is required for the cytoskeletal organization that leads to
197 myofibril growth.

198

199 **The *mylpfa*$^{-/-}$ mutant myofibril defect is rescued by *mylpfa-GFP* in a dose-**
200 **dependent manner**

201 The *mylpfa:mylpfa-GFP* transgene exhibits a wide range of expression levels, due in
202 part to positional effects from transposon insertion[39]. By combining the *mylpfa-GFP*
203 transgene with the *mylpfa*$^{-/-}$ mutant, we can test the correlation between Mylpf dosage
204 and fast-twitch myofibril growth within individual animals. We hypothesized that wild-
205 type animals produce Mylpf protein close to its saturation point, where additional protein
206 does not improve myofibril formation, but that the *mylpfa*$^{-/-}$ mutant produces Mylpf well
207 below this saturation point. Consistent with our prediction for the mutant, we see linear
208 correlation between GFP brightness and myofibril width in the *mylpfa*$^{-/-}$ mutant (Figure
209 3G). Consistent with our prediction for wild-type, we find a slight upward trend, but no
210 significant increase, in myofibril width in wild-type animals that express the *mylpfa-GFP*
211 transgene (Figure 3G). To confirm that myofibril size correlates with GFP brightness, we
212 also examined somite muscle in cross-section and used image thresholding to quantify
213 the myofibril cross-sectional area within the somite (Figure 3H-K). As expected, the
214 overall muscle cross-sectional area does not change in the *mylpfa*$^{-/-}$ mutant or in
215 transgenic animals, because *mylpfa* is required to localize proteins within muscle, not
216 for muscle growth (Figure 3H). Also as predicted, the cross-sectional area of myofibrils
217 is reduced in the *mylpfa*$^{-/-}$ mutant and restored by the *mylpfa-GFP* transgene to a
218 degree linearly correlated with GFP brightness (Figure 3I-M). Together these findings
219 suggest that Mylpfa expression restores the *mylpfa*$^{-/-}$ mutant proportionate with dosage,
220 but added Mylpfa has little impact on the wild-type animal.

221

222 **Expression of *mylpfb* restores myofibril formation in the *mylpfa*$^{-/-}$ mutant**

223 The differential requirement for *mylpfa* versus *mylpfb* in myofibril formation could be
224 explained either by differences in expression levels or coding sequence. To test the
225 efficiency of *mylpfb* in promoting myofibril growth, we generated a transgenic construct
226 that expresses *mylpfb-GFP* under the *mylpfa* promoter, *tg(mylpfa:mylpfb-GFP)*. The
227 *mylpfb-GFP* fusion protein localizes to the A-band of the wild-type myofibril and enables
228 F-actin to localize in sarcomeric repeats efficiently in the *mylpfa*$^{-/-}$ mutant; similar

229 localization is seen in animals mosaic for the *mylpfa-GFP* construct (Figure 4A-E). Both
230 constructs have a similar ability to restore myofibril structure in the *mylpfa*$^{-/-}$ mutant
231 (Figure 4F). The average localization of GFP to the myofibril is lower for Mylpfb-GFP
232 compared to Mylpfa-GFP, but the difference is not statistically significant (Figure 4F).
233 The Mylpfb-GFP brightness correlates linearly with myofibril width, with a slope similar
234 to Mylpfa-GFP (Figure 4G). To confirm these mosaic findings, we established germline-
235 inherited transgenic lines for *tg(mylpfa:mylpfa-GFP)mai102* and *tg(mylpfa:mylpfb-*
236 *GFP)mai103*. Both constructs rescue the *mylpfa*$^{-/-}$ mutant with similar trendlines, though
237 the *mylpfb-GFP* transgene has lower peak brightness than the *mylpfa-GFP* transgene
238 (Figure 4H). These findings support our hypothesis that the two zebrafish Mylpf genes
239 differ primarily by their expression levels.
240

241 **Early protein abundance correlates with *mylpfa* and *mylpfb* gene requirements in**
242 **fast-twitch myofibrils**

243 To further investigate how Mylpf gene dosage influences myofibril size, we examined
244 somite muscle structure in both homozygote and heterozygote offspring of the
245 *mylpfa*$^{+/-}$*;mylpfb*$^{+/-}$ heterozygous incross at 48 hpf. As expected, slow-twitch muscle
246 structure is normal across the *mylpfa* and *mylpfb* mutant combinations at this stage
247 (Figure 5A-D). Myofibrils are normal in the *mylpfb*$^{-/-}$ mutant fast-twitch muscle, severely
248 defective in the *mylpfa*$^{-/-}$ mutant, and completely lost in the *mylpfa*$^{-/-}$*;mylpfb*$^{-/-}$ double
249 mutant (Figure 5E-J). In the double mutant, both F-actin and MyHC are scattered
250 throughout the cytoplasm of the fast-twitch muscle cell, suggesting that even the pre-
251 myofibrils may eventually break down in this genotype (Figures 5H', S5). To investigate
252 how well these phenotypes map to Mylpf dosage, we plotted the correlation between
253 myofibril width and the Mylpf dosage, calculated by number of alleles skewed 6:1 for the
254 relative protein abundance at 1 dpf. We find a linear relationship between myofibril width
255 and predicted Mylpf dosage between the *mylpfa*$^{-/-}$*;mylpfb*$^{-/-}$ double mutant (0% dose)
256 and the *mylpfa*$^{+/-}$*;mylpfb*$^{+/-}$ double heterozygote (50% dose), with lessening effect at
257 higher dose (Figure 5J). Consistent with dose-dependent function, the *mylpfa*$^{+/-}$*;mylpfb*$^{+/-}$
258 double heterozygote shows modestly reduced myofibril width in fast-twitch muscle fibers
259 at 48 hpf (Figure 5I, J orange). The *mylpfa*$^{-/-}$*;mylpfb*$^{+/-}$ homozygote-heterozygote

260 combination has a sarcomere defect indistinguishable from the doubly homozygous
261 mutant, *mylpfa*$^{-/-}$;*mylpfb*$^{-/-}$ (Figure 5I, J green) suggesting a minimal threshold of Mylpf
262 dosage is needed for any myofibril assembly. We find similar trends by calculating the
263 sarcomeric fraction of MyHC and F-actin in these 48 hpf images (Figure 5K, S5). The
264 correlates persist at 72 hpf, suggesting that the dose effects are constant through
265 embryonic development (Figure 5L, M). Further support for sarcomere loss is seen
266 using TEM at 72 hpf, where the *mylpfa*$^{-/-}$;*mylpfb*$^{-/-}$ double mutant fast-twitch muscle
267 shows only a scattering of thick filaments and I-Z-I bodies and no myofibrils (Figure 5N-
268 P). Quantification of TEM images at 72 hpf is consistent with findings from
269 immunofluorescence (Figure S5). Together with our expression analysis, these findings
270 suggest that the Mylpf expression levels at 1 dpf predict the extent of myofibril formation
271 in somite muscle at 2 and 3 dpf.
272
273 ***mylpfa and mylpfb* are essential to MyHC localization, but not F-actin localization,**
274 **during early myofibril growth**
275 Our analysis at 2 and 3 dpf revealed that Mylpf function is required for myofibril
276 structure, but did not clarify which step of myofibril formation is regulated by Mylpf. We
277 hypothesized that sarcomeres may be disordered in the *mylpfa*$^{-/-}$ mutant because of an
278 initial defect in MyHC localization, independent of initial F-actin ordering. We examined
279 the *mylpfa*$^{+/-}$;*mylpfb*$^{+/-}$ heterozygous incross at a stage (26 hpf) when fast-twitch
280 myofibrils have recently begun to thicken. Wild-type and *mylpfb*$^{-/-}$ mutant siblings have
281 normal myofibrils at this early stage, (Figure 6A-B'), consistent with the low abundance
282 of *mylpfb* at 24 hpf. However, the *mylpfa*$^{-/-}$ mutant fails to properly localize MyHC to the
283 fast-twitch muscle cell's periphery where pre-myofibrils are forming (Figure 6C-C'). The
284 localization defect is even more severe in the *mylpfa*$^{-/-}$;*mylpfb*$^{-/-}$ double mutant,
285 suggesting that *mylpfb* also contributes to early myofibril formation (Figure 6D-D'). Since
286 myofibrils normally form at cell peripheries, we assessed localization by quantifying how
287 far the F-actin and MyHC labels spread into the central cytoplasm of fast-twitch muscle
288 cells (Figure 6E). As expected, F-actin and myonuclei are positioned normally within the
289 cell in all genotypes examined (Figure 6F, G), consistent with models that actin
290 localization precedes thick filament localization [5]. MyHC is also localized at cell

291 peripheries in the wild-type embryo, but MyHC spreads evenly through the cytoplasm of
292 the *mylpfa*$^{-/-}$;*mylpfb*$^{-/-}$ double mutant (Figure 6H). Similarly, the sarcomeric fraction
293 shows a severe MyHC defect but only a subtle change in F-actin localization in the
294 *mylpfa*$^{-/-}$;*mylpfb*$^{-/-}$ double mutant at 26 hpf (Figure S5). These findings suggest that
295 Mylpfa and Mylpfb together are essential to localize MyHC to the fast muscle cell's
296 periphery where the thick filaments interdigitate with pre-myofibrils to initiate myofibril
297 growth.
298
299 **The zebrafish larva compensates for impaired fast-twitch myofibrils by moving**
300 **slowly more often**
301 Zebrafish movement is driven largely by force generated in somite muscle [27]. The
302 zebrafish *mylpfa;mylpfb* knockout series allows us to investigate how fast-twitch
303 myofibril growth impacts swimming behavior. Our prior work showed that *mylpfa* is
304 essential to muscle strength and fish movement, leading to a severely impaired escape
305 response[35]. In further support, high-speed imaging shows that the sharp flexure driving
306 initial escape response (the 'C-bend') is consistently absent from this mutant (Figure 7A-
307 C, Video 1). To investigate whether these bursts of escape behavior are mirrored by
308 overall movements, we assayed overall behaviors for 25-minute sessions using
309 DanioVision, across the nine combinations of *mylpfa* and *mylpfb* zygosity at 6 dpf
310 (Figure 7D-I). Consistent with the escape response defect, we find that the highest
311 speed of movement is reduced in all animals homozygous for *mylpfa*$^{-/-}$, which do not
312 swim faster than 70 mm/sec (Figure 7D, E). However, we were surprised to find that the
313 overall speed is not decreased in any of the *mylpfa*;*mylpfb* mutant combinations, which
314 travel at least as far as wild-type siblings during the imaging period (Figure 7F, G). The
315 *mylpfa*$^{-/-}$ mutant animals maintain a high average speed by increasing their frequency of
316 movement at slow speeds, 20-40 mm/sec (Figure 7H). These 6 dpf fish spend most of
317 their time stationary (Figure 7I), consistent with previous findings [40]. When they do
318 swim, the animals move slowly over 99% of the time, so even a slight increase in the
319 likelihood of slow movements can outpace the complete loss of high-speed movement
320 (Figure 7I, J). Both slow and fast movements increase in heterozygous combinations,
321 such as the *mylpfa*$^{+/-}$;*mylpfb*$^{+/-}$ double heterozygote, which on average swims a little

322 further than its wild-type sibling (Figure 7F-J). The compensatory movement in the
323 *mylpfa*$^{-/-}$ mutant may cause or result from hypertrophy of slow-twitch myofibers (Figure
324 7K-M). Together these findings suggest that fast-twitch muscle function is only required
325 for the swiftest movements and that slower movements increase when the fast-twitch
326 muscle is compromised.
327

328 **Myofibril structure is disrupted by the expression of disease-causing MYLPF**
329 **alleles**

330 Missense alleles of human MYLPF cause DA [35], but it remains unclear how these
331 alleles impact myofibril formation. We hypothesize that these alleles may be
332 antimorphic, inverting the correlations between dosage and myofibril width. We tested
333 the functional impact of the DA-causing variants using plasmids that encode GFP-
334 tagged MYLPF protein variants, driven by the *mylpfa* promoter (Figure 8). We made
335 three plasmids with different MYLPF alleles: the typical allele ('WT'), a dominant allele
336 encoding p.Gly163Ser ('G163S'), which affects a residue that directly contacts MyHC,
337 and a recessive allele encoding p.Cys157Phe ('C157F') that affects a residue buried
338 within the MYLPF protein (Figure 8A) [35]. When expressed brightly, the WT *MYLPF-GFP*
339 allele restores myofibril formation in the *mylpfa*$^{-/-}$ mutant, indicating that function is
340 conserved between zebrafish and human (Figure 8B-D). Mosaic expression of the
341 C157F *MYLPF-GFP* mildly reduces myofibril width in wild-type fish but can partially
342 rescue width in the *mylpfa*$^{-/-}$ mutant, suggesting that it has reduced activity and a slight
343 antimorphic effect (Figure 8B, E, F). The G163S *MYLPF-GFP* allele cannot rescue the
344 *mylpfa*$^{-/-}$ homozygote at 48 hpf and partially narrows myofibrils in the wild-type siblings
345 (Figure 8B, G, H), suggesting that it has no positive function and some antimorphic
346 activity. The G163S variant is mildly detrimental to both wild-type and mutant myofibrils,
347 with increasing effect at high dosage (Figure 8I). In all cases, the shifts in myofibril width
348 correlate well with GFP brightness, such that in the *mylpfa*$^{-/-}$ mutant WT MYLPF-GFP
349 increases width, the C157F allele does so less efficiently (Figure 8I). The activity of
350 these DA-causing alleles in zebrafish is consistent with their inheritance in humans
351 since the more disruptive variant, G163S, causes DA as a heterozygote while the
352 partially functional variant, C157F, causes DA only when homozygous.

Discussion

The task of linking gene and protein dosage to phenotype is typically complicated by dynamic expression patterns and post-transcriptional regulation. Our experiments suggest that both Mylpf genes in zebrafish behave in a manner predicted by a straightforward interpretation of the central dogma. They each produce a single transcript in a single cell type and their transcriptional levels match their relative protein dosage. Gene copy number alone is a poor predictor of Mylpf knockout phenotype, because animals with very different phenotypes (*mylpfa*$^{-/-}$, *mylpfb*$^{-/-}$, and *mylpfa*$^{+/-}$*;mylpfb*$^{+/-}$) carry two mutant alleles of Mylpf and 50% of the normal wild-type alleles. However, we can accurately predict knockout phenotypes when we scale gene copy number by the relative dosage of Mylpfa and Mylpfb protein 24 hpf (6:1) (Figure 8J). Western blotting suggests there is little genetic compensation by Mylpfb in the *mylpfa*$^{-/-}$ mutant, nor much change in native protein levels when Mylpfa-GFP is expressed. We have not been able to test for the presence of the Mylpfb band in the *mylpfb*$^{-/-}$ mutant which cannot be behaviorally sorted from wild-type siblings. Instead, knockout and transgenic rescue studies suggest that Mylpf dosage and phenotype are co-linear between 0% (*mylpfa*$^{-/-}$*;mylpfb*$^{-/-}$) and 50% (*mylpfa*$^{+/-}$*;mylpfb*$^{+/-}$) of the wild-type dose, with diminishing returns at higher expression. The shape of this response curve suggests that Mylpf function in the wild-type embryo sits near or slightly above the saturation point for protein function. Consistent with wild-type saturation, introduction of an extra gene copy (the *mylpfa:mylpfa-GFP* transgene) causes little or no increase in myofibril width in the *mylpfa*$^{+/+}$ wild-type embryo. When beginning from a lower dose (the *mylpfa*$^{-/-}$ mutant), myofibril width can be restored to a degree linearly correlated with Mylpfa-GFP and Mylpfb-GFP protein abundance. We suggest that the dosage effects may not be limited to zebrafish, because human MYLPF-GFP rescues the *mylpfa*$^{-/-}$ mutant as efficiently as the zebrafish genes do. However, the dosage-phenotype correlate is lessened or reversed when we introduce MYLPF protein variants that cause DA, suggesting that normal activity level is vital to MYLPF protein function (Figure 8I, J).

383 Together, these findings poise the two zebrafish Mylpf genes as excellent models for
384 investigating a direct link from gene copy number and mRNA expression levels to
385 protein dosage and myofibril phenotype in the embryo.
386
387 Our work suggests that Mylpf controls myofibril organelle size without affecting overall
388 cell size. We propose that the cell uses Mylpf dosage to regulate localization of MyHC
389 to cell peripheries, particularly in situations where Mylpf abundance is limiting. These
390 limiting situations arise in the *mylpfa*$^{-/-}$ mutant but may also be present in the wild-type
391 animal during rapid growth. At least three mechanisms could explain the impact of Mylpf
392 on MyHC localization. First, since Mylpf is classically thought to stabilize contractile
393 MyHC, the thick filaments deficient in Mylpf protein may be marked as
394 misfolded/defective, triggering the mis-localization and myofibrillar defects [41]. Second,
395 once incorporated into myofibrils, RLCs continue to have known roles in muscle
396 contraction, such as increasing myosin step size leading to enhanced actin movement
397 [14,42]. Impaired step size is expected to reduce muscle force, which would reduce the
398 tension-driven elements of myofibril growth [7,10]. Third, Mylpf may act on non-contractile
399 myosin to mediate thick filament localization. For instance, RLC proteins are known to
400 bind to *myo18b*, an ATPase-deficient MyHC that stabilizes myosin-actin interactions
401 [13,43]. Consistent with this model, the zebrafish *myo18b*$^{-/-}$ mutant shows myofibril
402 formation defects similar to the *mylpfa*$^{-/-}$ mutant [44,45]. Future work to determine precisely
403 how Mylpf regulates myofibril growth may provide new ways to enhance muscle growth
404 after exercise and/or restore it during disease, without requiring cellular hypertrophy.
405
406 The DA gene variants may have antimorphic effects on muscle. The C157F DA allele is
407 recessively inherited in humans [35] and only causes a modest loss of function in early
408 zebrafish development. The G163S allele is dominantly inherited in humans [35] and
409 causes severe loss of function in early zebrafish development. Our results suggest that
410 both variants are antimorphic because both alleles decrease myofibril widths in the wild-
411 type embryo, proportionate with protein dosage. Our model is consistent with recent
412 proposals that most DA-causing alleles may have antimorphic effects [25]. Antimorphs
413 can arise by either gain or loss of protein function, as was established initially using

414 actin alleles in *Drosophila* [46]. For example, a DA-causing *MYH3* allele was recently
415 shown to increase Myosin activity, leading to hypercontraction and disease, in an
416 antimorphic gain-of-function manner [47]. The DA-causing MYLPF alleles may have
417 antimorphic effects through loss of function, by competing with wild-type MYLPF for
418 binding sites in thick filaments. However, the distinction between loss and gain of
419 function is muddled in these animals. Complete loss of Mylpf function leads to complete
420 loss of fast-twitch myofibrils but it also increases slow-twitch muscle size and causes a
421 gain of low-speed movement (Figure 8J, blue text). We have not yet assessed the
422 behavioral impacts of DA-causing alleles, to learn if animal activity is increased or
423 decreased, because the mosaic fish are labeled too sparsely to assess behavioral
424 changes. Subsequent work using stable transgenes may help elucidate why the DA-
425 causing alleles are antimorphic and may also reveal their impact on behavior.
426
427 Over 95% of zebrafish somite muscle is fast-twitch at 6 dpf, so we did not expect the
428 *mylpfa*$^{-/-}$*;mylpfb*$^{-/-}$ double mutant zebrafish to move as far through time as their wild-type
429 siblings while using only ~5% of the normal myofibril volume. The zebrafish *mylpfa*$^{-/-}$
430 mutant behaves as expected on short timescales, producing force that is reduced in
431 proportion to the decreased myofibril cross-sectional area [35]. Likewise, *mylpfa*$^{-/-}$ mutant
432 fish lack C-bends, have overall muscle weakness, and show an impaired escape
433 response consistent with other fast-twitch deficient fish [35,48,49]. However, the same
434 animals generate slow movements more frequently within the course of our 25-minute
435 experimental window, eventually moving as far as their wild-type siblings. Partial loss of
436 Mylpf function could even increase total movement, since the *mylpfa*$^{+/-}$*;mylpfb*$^{+/-}$ double
437 heterozygote tends to move even further than wild-type siblings. Consistent with our
438 findings, another group recently showed that zebrafish lacking fast-twitch acetylcholine
439 receptors upregulate slow-twitch synapses and behaviors by adult stages [48]. However,
440 this slow-twitch compensation has not previously been observed in larvae and we do
441 not know if there is synaptic compensation in Mylpf mutant zebrafish. The behavioral
442 compensation in Mylpf-deficient animals may be purely due to changes in muscle. Over-
443 reliance on slow-twitch fibers may act as a form of exercise, leading to the observed
444 slow-twitch hypertrophy [28], which in turn should strengthen slow-twitch movement. The

importance of muscle hypertrophy and neural activity could be resolved by investigating muscle strength, calcium signaling, and synapse morphology through time in Mylpf mutants.

Collectively, our findings suggest that Mylpf dosage controls myofibril size, with profound effects on muscle structure and function in zebrafish. *Mylpf* mRNA abundance is enriched in the fast-twitch muscle of farmed mammals that have very tender meat, suggesting that it may be a target of selection on farms [50]. These meat quality factors are predicted by point mutations in the Mylpf promoter region [51]. Likewise, the abundance of *Mylpf* mRNA is a hallmark of muscle differentiation and required for this process [52]. Although the mouse *Mylpf*$^{+/-}$ heterozygote does not have muscle impairment after birth, prenatal muscle disorder has not been ruled out [22]. Mylpf gene dosage does impact muscle development in insects since *Drosophila* heterozygous for RLC mutation has impaired myofibril assembly in fast-twitch flight wing muscle [17]. In some cases, increased light chain activity may also promote new myofibril formation. For instance, activation of cardiac myosin light chain kinase is necessary and sufficient to initiate the formation of sarcomeres in cultured heart cells [53]. These findings lead us to propose that Mylpf abundance is a ripe target for heterometric selection, which alters the prevalence of alleles in a population based on how the alleles affect a gene's expression level. Given how widespread this effect seems to be, the sensitivity of myofibril size to Mylpf dosage may have applications in many contexts where myofibril growth is desired, including exercise physiology, farming, and human health.

Acknowledgements

The fish facilities at the University of Maine fish facility and The Ohio State University (OSU) provided excellent animal care. Dr. Joy-El Talbot from Iris Data Solutions developed an ImageJ macro for sarcomere fraction quantification. Dr. April DeLaurier provided feedback in the writing process. Dr. Clarissa Henry generously provided mentorship and resources to the Talbot lab. Dr. Thomas Gallagher and Collin Whitlock facilitated data sharing between OSU and the University of Maine. Paula Monsma and Dr. Sarah Cole supported imaging on the electron and confocal microscopes at The Ohio State University. This project was supported by a University of Maine Institute of Medicine Seed Grant, and NIH grant R15AR081019 to JCT, NIH R15GM140409 to JBK, by NIH grants GM088041 and GM117964 to SLA, and COBRE P20GM144265-01A1 to JBK and JCT.

Conflict of Interest Statement: The authors declare that they have no competing interests.

Materials and Methods

Zebrafish husbandry and established strains

Fish strains were maintained using standard methods [54]. All animal protocols used in this study were approved by the Institutional Animal Care and Use Committees at The Ohio State University (2012A00000113) and the University of Maine (A2022-09-05). Embryo/larval staging followed established metrics [55]. We genotyped the *mylpfa*^{oz30} 20 bp deletion allele [35] using primers (F 5'-TCTCTACAGGCCAGCTGAATG'3', R 5'-ACCCTTCAACTTCTCTCCGAAC'3') that amplify a 116 bp product in wild-type fish and a 96 bp product in the *mylpfa*^{oz30} homozygote. We genotyped the 1 bp *mylpfa*^{oz43} allele [35], using primers 5'- GCTTCATTGCTGTCAGGATAGAG-3' and 5'-ACCCTTCAACTTCTCTCCGAAC-3', followed by digestion with BsmFI restriction enzyme (NEB, New England Biolabs). The enzyme cuts the wild-type amplicon into two products of similar size (184 bp and 185 bp) and the mutant amplicon (368 bp) remains uncut. Homozygotes for both *mylpfa*^{oz30} and *mylpfa*^{oz43} can be consistently sorted from wild-type siblings based on pectoral fin immobility and by a distinctively slowed escape response. The new mutant and transgenic lines generated during this study are described below. Zebrafish lines in this study were maintained on the AB wild-type background.

Construction of *mylpfb*^{oz39}

The *mylpfb*^{oz39} mutation was generated using established CRISPR-Cas9 protocols [56]. One-cell embryos were co-injected with Cas9 mRNA and guide RNA targeting exon 2 (5'- GGAAAACAGTAAAGTTGATG -3'), raised to adulthood, and outcrossed to identify germline-transmitting founders. F1 progeny were screened using High-Resolution Melting Analysis (HRMA) (primers 5'-CCCTCTCTAAAACAAACAGGCTTTC-3' and 5'-GGTAAGTGAAGATTTGGACAACTC-3') to identify founders carrying a CRISPR-induced *mylpfb*^{oz39} lesion which caused a frameshifting 5 bp deletion. Genotyping for *mylpfb*^{oz39} used primers F 5'-GCAACAATGGGTCAGCTAATG-3' and R 5'-

513 CCCAAAACCAAAAGTATGAG-3', then PCR products were cut with BccI enzyme
514 (NEB) which cleaved the wild-type amplicon into two products (120 bp and 76 bp) while
515 mutant amplicon (191 bp) remained uncut. The lesion was confirmed via Sanger
516 sequencing of homozygotes and the founder was outcrossed for at least two
517 generations after CRISPR injection, before conducting the experiments shown.

518

519 **Transgene construction**

520 Plasmid and transgenic construction used traditional restriction enzyme based
521 molecular cloning methods. The five plasmids constructed for mosaic analysis in this
522 study are *pMylpfa:mylpfa-GFP*, *pMylpfa:mylpfb-GFP*, *pMylpfa:WT-MYLPF-GFP,*
523 *pMylpfa:C157F-MYLPF-GFP, and pMylpfa:G163S-MYLPF-GFP.* Briefly, we obtained
524 GeneArt-strings (Invitrogen) of the sequence encoding Mylpfa*,* Mylpfb*,* wild-type human
525 MYLPF*,* MYLPF p.Gly163Ser (G163S)*,* or MYLPF p.Cys157Phe (C157F) proteins.
526 These coding sequences were inserted into a plasmid containing the *mylpfa* promoter
527 flanked by TOL2 sites [36,57,58]; GFP was linked to the 5' end of Mylpf genes, connected
528 via a sequence encoding a short flexible peptide (GGGGSGAT). Plasmid injection was
529 accompanied by co-injection of zebrafish-optimized nuclear transposase ZT2TP [59,60].
530 For transient analysis, animals with high levels of mosaicism were selected for imaging
531 and all experiments were repeated on at least two independent injection days. Stable
532 transgenic lines were generated for the two zebrafish transgenes, Tg(*pMylpfa:GFP-*
533 *mylpfa*)*mai102*, and Tg(*pMylpfa:mylpfb-GFP*)*mai103*. For stable transgenic analysis, at
534 least two founders were analyzed per rescue construct.

535

536 **Immunohistochemistry and HCR ISH**

537 Whole mount immunohistochemistry used established markers and techniques [61].
538 Briefly, the larvae were fixed in 4% paraformaldehyde and washed in PBST (1X PBS,
539 0.1% Tween-20) before immunolabel. Embryos older than 1 dpf were gently
540 permeabilized using a brief treatment with 0.001% Proteinase-K, washed repeatedly in
541 PBST, then blocked for at least two hours in 0.5% TritonX, 1X PBS, 2% NSS, 4% NGS;

542 1% DMSO [61,62]. This is followed by overnight incubation at 4°C with primary antibodies
543 diluted in blocking solution. We used primary antibodies for the myonuclei (1:500,
544 Rbfox1l) [63]; Z-disk (1:500, α-actinin, Sigma, A7732); Myomesin [1:30, mMac,
545 Developmental Studies Hybridoma Bank (DSHB)] [64], MyHC (1:1000, A4.1025, DSHB)
546 [65], and Mylpf (1:2000, present study). The following day, larvae were washed 5-6 times
547 over 1 hour in PBST, and then incubated in secondary antibodies for 4 hours at room
548 temperature. Larvae were washed 6-8 times over 2 hours in PBST, mounted with 0.2%
549 agarose then imaged, or kept in PBST at 4°C prior to imaging. F-actin labeling uses
550 Alexa Fluor-conjugated phalloidin (1:50, Thermo Fisher), added in the final two hours of
551 the secondary antibody incubation. HCR ISH procedures use established protocols with
552 probes and amplifiers supplied by Molecular Instruments [66]. The *mylpfa* and *mylpfb*
553 genes are very similar to one another, so nine unique *mylpfa* probes and five unique
554 *mylpfb* probes could be generated, whereas we were able to generate twenty probes to
555 *myl10*. To compare HCR ISH signal intensity, separate fish were labeled with *mylpfa*
556 and *mylpfb* probes, both in the 488 nm excitation channel and then imaged with
557 matched confocal settings. HCR ISH images were quantified in FIJI using brightness
558 analysis within the fast-twitch region.

559

560 **Antibody production, validation on Western blot**

561 The zebrafish Mylpf antibody was generated by Boster Bio using zebrafish Mylpfa (AA
562 14 to 167 of NP_571263.1) in complex with a Mylpf-binding region that is found in
563 several MyHC proteins (RRESIYTIQYNIRSFMNVKHWPWMKVYYKIKPL). This mixture
564 was injected into rabbit via three rounds of injection, followed by column purification and
565 Elisa confirmation by Boster Bio. Western blot in the Talbot Lab, showed only one band
566 each for Mylpfa (16 kD) and Mylpfb (18 kD) and no label in the MyHC size (252 kD). For
567 western blotting, animals were raised to the desired stage, sorted by behavioral
568 phenotypes, then pools of 10 (72 hpf) to 40 (24 hpf) animals were homogenized using
569 0.5 mm zirconium beads (Laboratory Supply Network) in Bolt solution (Invitrogen). The
570 *mylpfa*$^{-/-}$ mutant animals were sorted by behavioral phenotypes and proper separation
571 was confirmed using PCR genotyping. Homogenized samples were run on a 4-20%

572 gradient acrylamide gel (Bio-Rad) or an “any kD” precast polyacrylamide gel (Bio-Rad).
573 The protein samples were transferred to Polyvinylidene difluoride (PVDF) membranes
574 (Millipore Sigma) followed by blocking solution (5% nonfat dry milk) overnight at 4˚C.
575 Membranes were incubated in primary antibody at room temperature for 1 hour,
576 followed by incubation in secondary antibody for 2 hours. The resulting fluorescence
577 was measured by scanning the blot with the Odyssey Infrared Imager (LICOR). The
578 Mylpfa to Mylpfb ratio was quantified using GelBox software [67] and FIJI [68]. Primary
579 antibodies included mouse polyclonal anti-MyHC (A4.1025, DSHB, 1:1000) to detect
580 MyHC protein while rabbit polyclonal anti-Mylpf (Boster, 1:1000) detected both Mylpfa
581 and Mylpfb protein. The secondary antibodies used are donkey-anti-mouse-800
582 (1:10000 dilution) and donkey-anti-rabbit-680 (1:10000 dilution).

583

584 **Protein modeling**

585 Mylpf proteins were modeled in complex with the binding region of Myhz1.3 (zebrafish)
586 or MYH3 (human) using Robetta [69] and then models were visualized using PyMol
587 (Schrödinger).

588

589 **Confocal imaging**

590 Confocal images in Figure S2 were collected using an inverted Nikon TiE microscope
591 equipped with an Andor Revolution WD spinning disk confocal system. All other
592 confocal images were acquired using a Leica TCS Sp8 confocal microscope and
593 processed with Lightning in LasX software. Myotomes were imaged over the mid yolk
594 tube region of embryos and larvae. Image settings including laser power and gain were
595 equivalent for compared groups and confocal export protocols were standardized for
596 each experiment.

597

598 **Sarcomeric fraction calculation**

599 To quantify the degree to which muscle proteins localize to sarcomeres, we developed
600 metric for analyzing how much protein analyzes to sarcomeric repeats, which we term

601 the sarcomeric fraction (Figure S3). This calculation begins by drawing Region of
602 Interest (ROI) lines along the length of a myofiber in ImageJ, measuring ten to thirty
603 ROIs per image. The grayscale intensities are exported from FIJI and the periodicity of
604 these intensities is determined using the 'distance between peaks' function in MATLAB.
605 Peak-to-peak distances per intensity were determined per image, and bootstrap
606 confidence intervals were calculated using variation between images, shown via
607 histogram to represent the Fraction of Peaks/micron (μm). We used distinct bin sets for
608 markers with full-sarcomere (F-actin, Myomesin, Actinin) or half-sarcomere length
609 (MyHC, Mylpf-GFP). Sarcomeric F-actin shows peak signals in the 0.7-1.1 μm range
610 and 1.55-2.3 μm range, reflecting the fact that most F-actin periods are sarcomere
611 length but sometimes a gap can be seen at the M-line. For consistency, we used this
612 same bin set for Myomesin and Actinin (Figure S3). Sarcomeric MyHC and Mylpf-GFP
613 show two peak signals in bins 0.6-1.2 μm and 1.75-2.05 μm (Figure S3), because these
614 proteins are usually subdivided into the two A-Bands, but sometimes blur together to the
615 length of a full sarcomere. The sarcomeric fraction is the ratio of image periodicity within
616 the sarcomeric length bin to the overall periodicity of that marker. Sarcomere fractions
617 were calculated per animal then subjected to further statistical tests using JMP
618 software.

619

620 **Quantifying protein localization within cells**

621 To quantify protein localization within muscle cells, we first imaged dorsal somites
622 muscle above the mid yolk tube with high Z-resolution (0.5 μm) and exported a
623 reconstructed cross-section through the somite. Then, a mask was drawn manually,
624 circling the borders of each cell. A custom MATLAB script determined image brightness
625 at each pixel, moving from the periphery of the cells to the center. These edge-center
626 distances were scaled to micron lengths, averaged, and bootstrap confidence intervals
627 were calculated across samples of a given genotype. Graphs with confidence intervals
628 were then overlaid for each genotype.

629

630 **Myofibril width measurements**

631 To measure myofibril width, we drew region of interest (ROI) lines across the narrow
632 axis of the myofibril in FIJI, typically measuring thirty myofibrils per image. For mosaic
633 animals we measured both GFP+ and non-transgenic myofibrils within the same single
634 confocal slice. Images were included only if they contained at least ten GFP+ myofibrils.
635 For stable transgenics lines, we compared measurements from non-transgenic and
636 transgenic siblings. We generated a custom FIJI macro to simplify measurement and
637 compile all measures from a given image. These measurements were averaged per
638 image using MATLAB and the averages were imported into JMP software for statistical
639 analysis.

640

641 **GFP brightness analysis**

642 Analysis of fluorescent brightness began during imaging, when we ensured that all data
643 meant for comparison was collected with equivalent settings, such as shared laser
644 power. We evaluated the GFP brightness using the mean grayscale value of the GFP
645 channel in FIJI software. For stable transgenic lines, we drew ROI around the full somite
646 at the center of each image, while excluding the superficial slow fibers. In mosaic
647 animals, we drew ROI around each muscle fiber because there was often a high level of
648 variation within a single image. A custom FIJI macro simplified the measurement of the
649 mean grayscale value of each image. Myofibrils are considered non-transgenic if the
650 GFP brightness is <1 (0-255), were and considered transgenic if in the 10-255 range.
651 MATLAB was used to calculate the average of each mean grayscale value per image
652 followed by statistical comparisons in JMP software.

653

654 **Transmission electron microscopy**

655 For TEM, embryos were raised to 72 hpf, fixed in glutaraldehyde, resin embedded, thin
656 sectioned, and contrasted using Uranyl acetate and Reynold's lead citrate before
657 imaging on a Tecnai 30 G2 TWIN microscope. At least three fish were examined per
658 genotype and multiple sections were imaged per fish. Statistical analysis was performed
659 using only one image per animal to ensure biological independence. Myofibril widths

660 and sarcomere fraction were determined using TEM images with magnification low
661 enough to examine variation across a half-somite.

662

663 **Behavioral analysis**

664 For tail curvature assessment, individual larvae were placed in a petri dish and prodded
665 with a piece of fishing line, imaged using a GoPro Hero camera with a mounting ring
666 (H12Pro, Back-Bone) set to 240 frames/sec. The frame with highest curvature was
667 transferred to FIJI and curvature was measured along the length of the trunk using the
668 Kappa plugin[70]. Total curvature was calculated by multiplying average curvature by the
669 length and then converting from Radians to Degrees. For speed analysis, larvae were
670 placed one per well into a 12-well plate with 3 ml of facility water at 6 dpf. Then, they
671 were imaged in a DanioVision system (Noldus) equipped with a magnifier for improved
672 resolution. The plates were incubated at 28˚C in the preheated chamber. The larvae
673 were imaged using the infrared wavelength every 0.33 seconds for a total of 25
674 minutes, cycling lights off and on every five minutes. Larvae were tracked using
675 EthoVision XT Version 15.0 video tracking software by Noldus. Distance traveled is the
676 sum of distances in this 25-minute time interval. Speed is calculated per 0.33 second
677 time interval and then binned into different speed ranges using Microsoft Excel
678 Histogram function. Speed bins were selected to best show movement dynamics by
679 speed while reducing noise caused by the rarity of movements at the highest speeds.
680 Analysis was limited to velocities under 200 mm/sec because video examination shows
681 that higher-speed measurements are indications of tracking glitches rather than actual
682 zebrafish movement. Shown plots (Figure 7D-J) integrate data collected from the
683 *mylpfb*$^{+/-}$ heterozygous incross, *mylpfa*$^{+/-}$;*mylpfb*$^{+/-}$ double heterozygous incross, and
684 outcrosses of *mylpfa*$^{+/-}$;*mylpfb*$^{+/-}$ to AB. Each set of crosses was replicated at least three
685 times with consistent results across experiments.

Figures and Legends

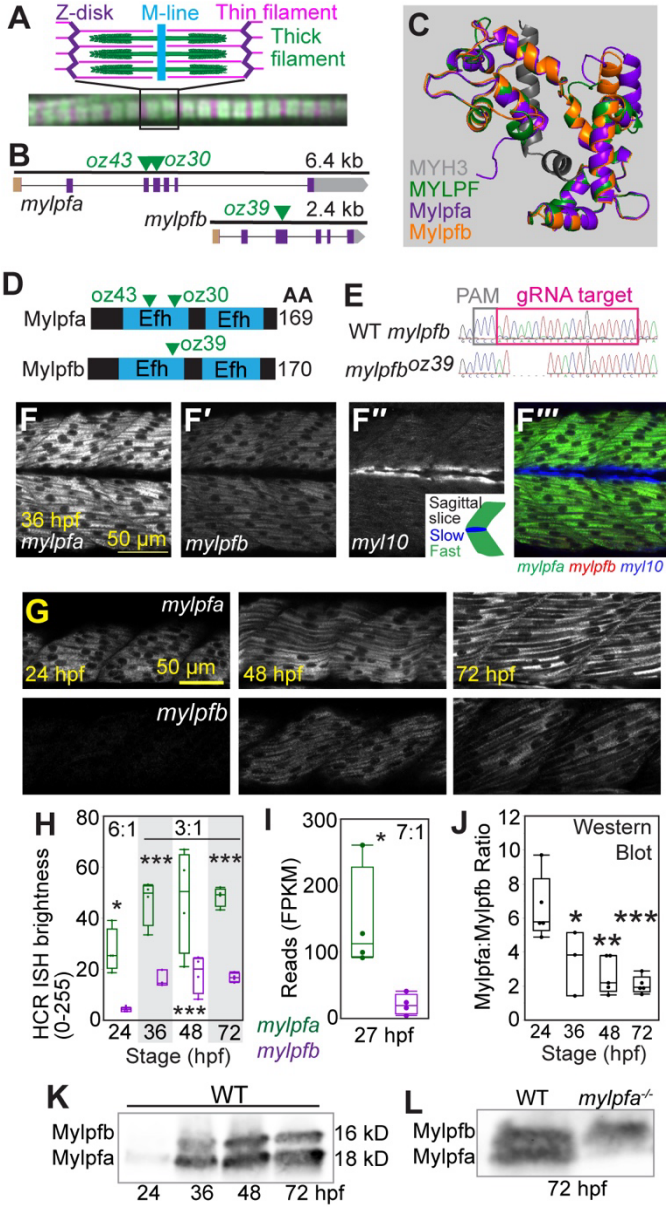

Figure 1: The *mylpfa* gene is expressed more abundantly than *mylpfb* in fast-twitch muscle. **(A)** Illustration of a sarcomere and an image of a fast-twitch myofibril at 26 hpf, with MyHC labeled green using A4.1025 and F-actin labeled magenta using phalloidin. **(B)** Illustration of *mylpfa* and *mylpfb* gene structure and the location of frameshifting alleles used in this study. Shown features include the 5' UTR (brown), coding sequence (purple), 3' UTR (gray), and frameshift locations (green arrows). **(C)** Overlay of predicted protein structures generated using Robetta, showing a high degree of expected similarity between zebrafish Mylpfa, Mylpfb, and human MYLPF proteins. **(D)** Illustration of Mylpfa and Mylpfb proteins, with arrowheads marking frameshift locations. **(E)** Chromatogram showing the gRNA target in wild-type sequence (top) and the 5 bp *mylpfb*^{oz39} lesion sequenced from a homozygous mutant (bottom). **(F-F‴)** HCR ISH imaged in somites over the mid-yolk tube of a 36 hpf embryo. Shown as a single channel for *mylpfa* (F), *mylpfb* (F') or the slow muscle marker *myl10* (F''), and as a merged image (F‴). **(G)** HCR ISH shows relative expression levels for *mylpfa* and *mylpfb* through embryonic development. **(H)** Box plot showing the brightness of *mylpfa mylpfb* in the HCR ISH images, with *mylpfa*:*mylpfb* ratios shown per time-point. **(I)** FPKM values for *mylpfa* and *mylpfb* at 27 hpf, from a previously reported RNA-seq dataset [38]. **(J)** Ratio of Mylpfa to Mylpfb band intensity in western blot; points represent biological replicates of pooled animals. **(K)** Image of a western blot showing Mylpfb and Mylpfa protein abundance at 24, 36, 48, and 72 hpf. **(L)** Western blot showing Mylpfb and Mylpfa protein in the wild-type and the *mylpfa*$^{-/-}$ mutant which lacks the Mylpfa band. Significance threshold determined by Tukey-Kramer comparison after one-way ANOVA; * P<0.05, ** P<0.01. Scalebar in F is for F-F‴.

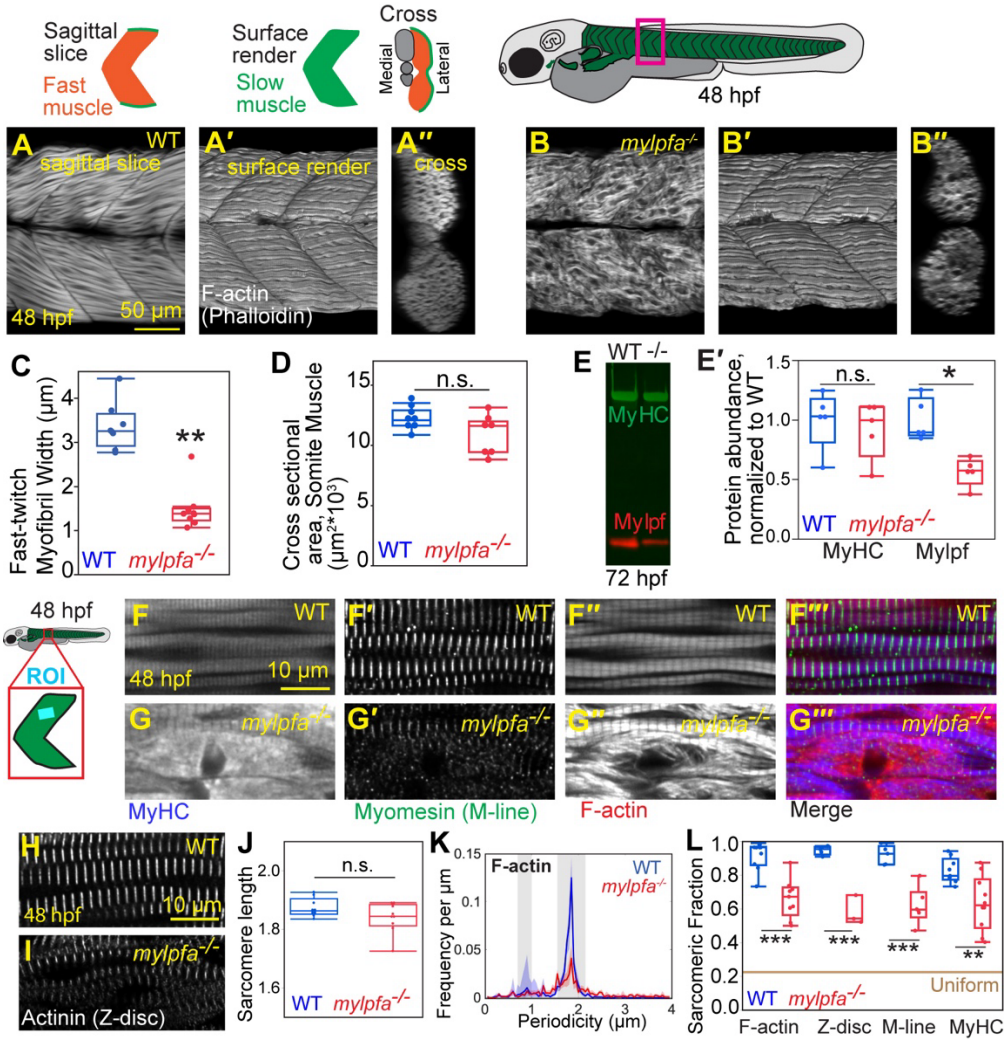

Figure 2: Zebrafish *mylpfa* is necessary for fast-twitch myofibril formation. **(A-B")** Three views of somites are illustrated above (A) and imaged in a wild-type animal and *mylpfa*$^{-/-}$ mutant sibling, each imaged at 48 hpf. **(C)** Box plot of myofibril width, measured from the sagittal confocal slice. **(D)** Plot of muscle cross-sectional area (CSA) measured from the orthogonal view of confocal stacks from the wild-type and *mylpfa*$^{-/-}$ mutant siblings. **(E)** Example of a western blot for MyHC and Mylpf, including Mylpfa and Mylpfb, in the wild-type (WT) and the *mylpfa*$^{-/-}$ mutant (-/-) samples at 72 hpf, with (**E'**) quantification shown as a box plot. **(F-G''')** Fast muscle myofibers, labeled at 48 hpf, showing co-label for MyHC (A4.1025), M-line (anti-Myomesin), and F-actin (phalloidin), shown as single channel or overlays. **(H, I)** Actinin label on comparable samples. **(J)** Box plot of sarcomere lengths in the *mylpfa*$^{-/-}$ mutant and their wild-type siblings, showing no change in length. **(K)** Plots showing that the *mylpfa*$^{-/-}$ mutant shows reduced F-actin sarcomeric periodicity (gray bars). Lightly colored regions indicate bootstrap confidence intervals. **(L)** Box plot showing sarcomeric fraction for each marker, calculated on a 0-1 scale, as described in Figure S3. Throughout the figures, the wild-type plots are blue and the *mylpfa*$^{-/-}$ plots are red. Points within box plots represent the individual animals or a single western blot image. Scalebar in A is for A-B", in F is for F-G'''', in H is for H, I. Significance thresholds determined by Tukey-Kramer HSD comparisons after one-way ANOVA: not significant (n.s.) is P>0.1, * P<0.05, ** P<0.01, *** P<0.001.

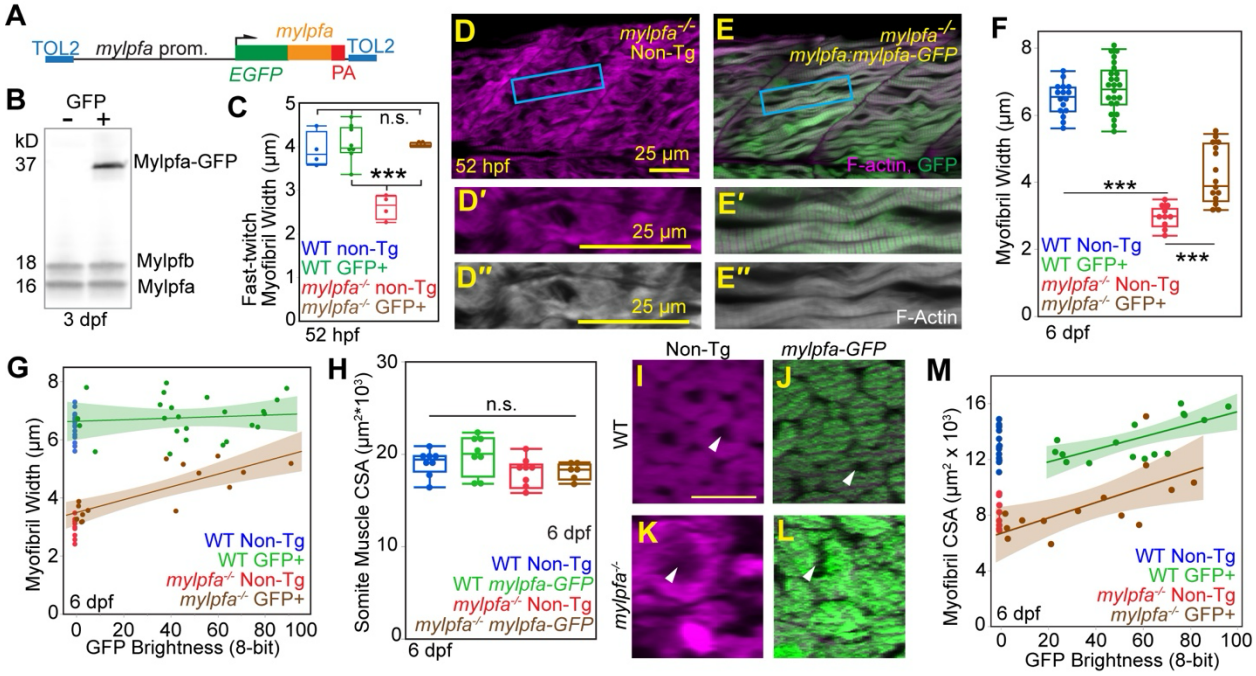

Figure 3: A *mylpfa:mylpfa-GFP* transgene rescues the *mylpfa*$^{-/-}$ mutant. **(A)** Schematic illustrating the *mylpfa:mylpfa-GFP* transgene. **(B)** Western blot of Mylpf protein from the wild-type fish at 3 dpf, and their GFP+ siblings shows that the transgene produces one thin band that is shifted upwards by the addition of GFP. **(C)** Box plot showing the effect of *mylpfa:mylpfa-GFP* transgene expression on the myofibril width at 52 hpf. **(D, E)** Confocal slice through fast-twitch muscle in a non-transgenic (Non-Tg) phalloidin labeled *mylpfa*$^{-/-}$ mutant (D) or a *mylpfa:mylpfa-GFP* transgenic sibling mutant (E) at 52 hpf. **(D', E')** Zoomed view showing myofibril structure. **(D'', E'')** The phalloidin channel showing myofibrils unobscured by GFP. **(F)** Box plot showing myofibril widths in zebrafish at 6 dpf. **(G)** Scatterplot showing correlations between GFP brightness and myofibril width at 6 dpf. **(H)** Box plot of total somite muscle cross-sectional area measurements at 6 dpf, taken from orthogonal views of confocal stacks. **(I-L)** Examples of cross-sectional images, reconstructed from confocal stacks. The myofibril-free central region (Arrowhead) of non-transgenic wild-type muscle (I) is sometimes reduced in the transgenic animal (J). This central area expands in the non-transgenic *mylpfa*$^{-/-}$ mutant (K) but is reduced in the *mylpfa*$^{-/-}$ mutant carrying the transgene (L). **(M)** Scatterplot showing correlations between myofibril cross-sectional area and GFP brightness. Scalebars in D-D''' is for E-E''', in I is for I-L. Significance thresholds are determined by Tukey-Kramer HSD comparisons after one-way ANOVA: ** indicates P<0.01, *** P<0.001, n.s. P>0.1.

Figure 4: Expression of either *mylpfb-GFP* or *mylpfa-GFP* can rescue the *mylpfa*$^{-/-}$ myofibrils. **(A-D)** Images of phalloidin labeled animals at 72 hpf showing mosaic expression of the *mylpfa:mylpfa-GFP* (A, B) or the *mylpfa:mylpfb-GFP* transgene (C, D). **(E)** Box plots showing the fraction of F-actin localized to sarcomeres, calculated in non-transgenic muscle fibers and GFP+ muscle fibers within the same mosaic animals. **(F)** Box plots showing the sarcomeric fraction for GFP. **(G)** Scatterplot showing the correlation between GFP brightness and myofibril width in *mylpfa*$^{-/-}$ mutant animals carrying *mylpfa:mylpfa-GFP* or *mylpfa:mylpfb-GFP* transgenes. Linear correlates for the two transgenes have overlapping confidence intervals. The vertical brown line indicates animals classified as transgenic vs. non-transgenic. **(H)** Scatterplot of myofibril widths in animals bearing an inherited transgene. Scalebar in A applies to A-D. Significance: n.s. is P>0.1, *** indicates P<0.001 as determined by Tukey-Kramer HSD comparisons after one-way ANOVA.

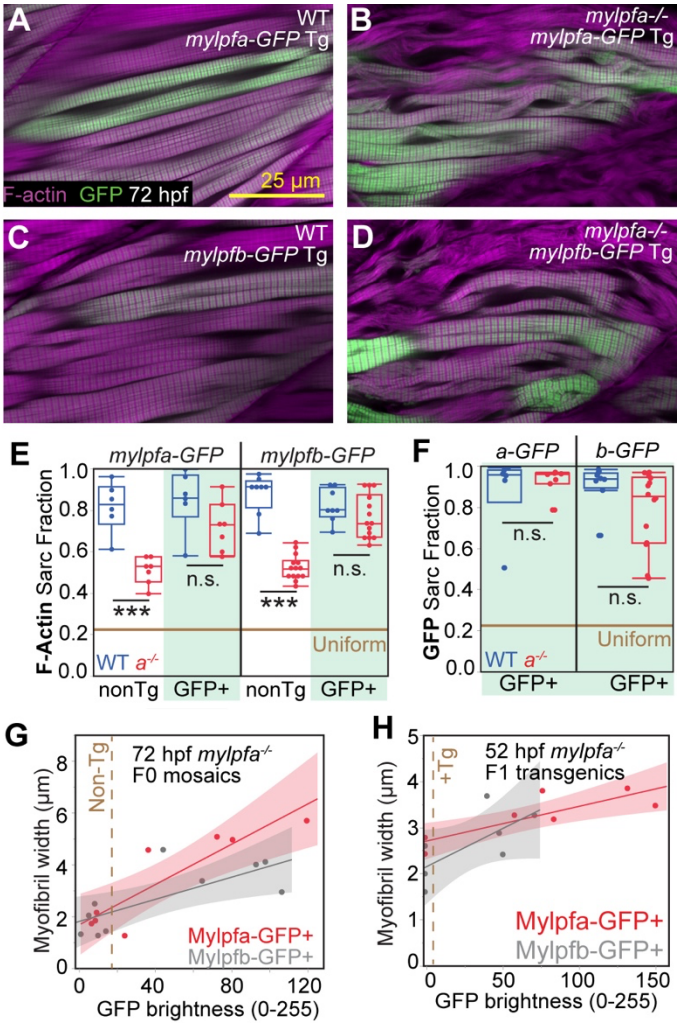

Figure 5: Levels of myofibril formation correspond to dosages predicted by *mylpfa* and *mylpfb* loss of function. **(A-D)** 3D renders of confocal stacks show normal myofibril structure in slow muscle fibers across Mylpf genotype. **(E-H)** Medial slices show a portion of myotome rich in fast-twitch fibers, with robust myofibrils in the wild-type sibling (E) and the *mylpfb*$^{-/-}$ mutant (F), but overt myofibrillar defect in the *mylpfa*$^{-/-}$ mutant (G) and total loss of myofibrils in the *mylpfa*$^{-/-}$;*mylpfb*$^{-/-}$ double mutant (H). Zoomed images show myofibrillar structure within fast-twitch muscle fibers (E'-H'). **(I)** Box plots of myofibril widths in slow-twitch and fast-twitch muscle. Slow and fast-twitch widths plotted separately because the slow-twitch fibers were measured on 3D rendered images and the fast-twitch fibers were measured on confocal slices. **(J)** Scatterplot showing the same myofibril width data from fast-twitch muscle (in I) replotted as a correlate with predicted protein dosage at 24hpf, with each allele scaled 6:1 for Mylpfa:Mylpfb ratio. **(K)** Box plots showing the fraction of sarcomeric MyHC localization. **(L)** Box plots showing myofibril widths in 72 hpf phalloidin-labeled animals. **(M)** Scatterplot of the same data with each allele scaled 6:1 for Mylpfa:Mylpfb. **(N-P)** Transmission electron microscopy showing normal sarcomere structure in the wild-type sibling (N), partial sarcomeric disarray in the *mylpfa*$^{-/-}$ mutant (O) and only scattered sarcomeric components in the *mylpfa*$^{-/-}$;*mylpfb*$^{-/-}$ double mutant (P). Scale bars in D, H, and H' are 10 µm, applicable to their row. Scale bar in N is 1 µm. Significance thresholds: not significant (n.s.) is P>0.1, ** P<0.01, *** P<0.001 as determined by Tukey-Kramer HSD comparisons after one-way ANOVA.

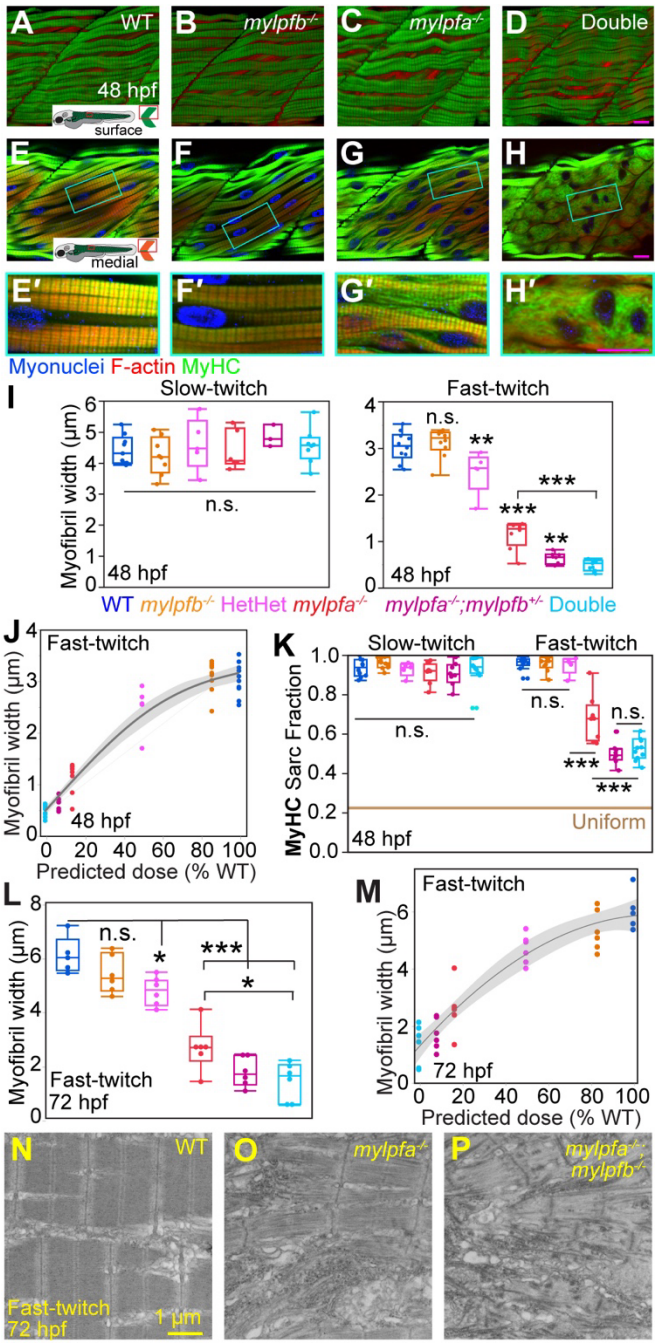

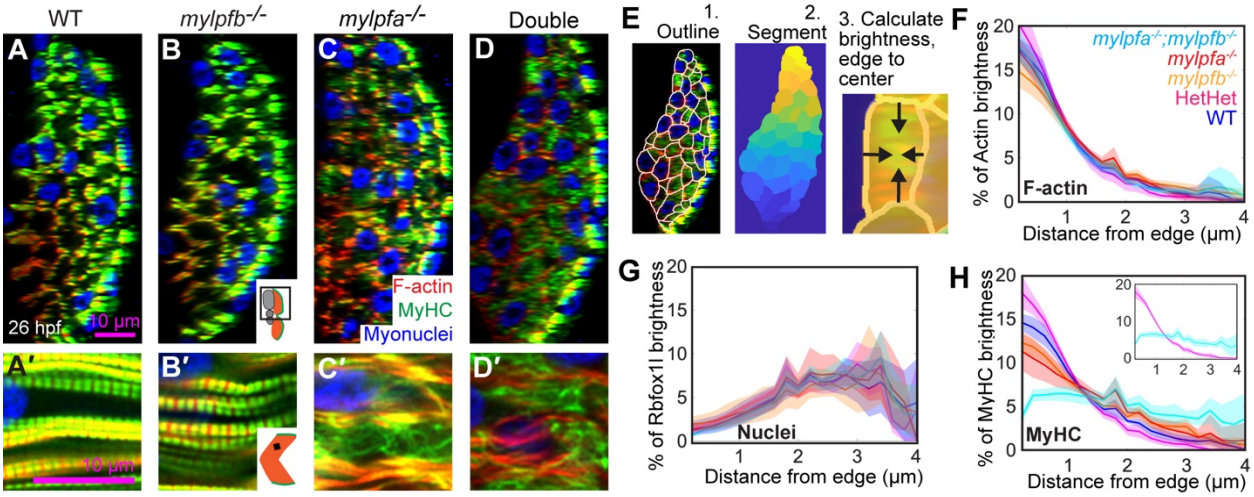

Figure 6: <u>*mylpfa* and *mylpfb* are required for myosin heavy chain localization in young myofibers.</u> **(A-D)** Immunolabel of fast muscle fibers at 26 hpf shown as orthogonal views of Z-stacks of wild-type (A), *mylpfb*$^{-/-}$ (B), *mylpfa*$^{-/-}$ (C), and *mylpfa*$^{-/-}$*;mylpfb*$^{-/-}$ double mutant zebrafish (D). **(A'-D')** Zoomed sagittal views of the same animals. **(E)** Overview of protocol to measure image brightness from edge-to-center. The fast-twitch muscle cells are (1) manually outlined, (2) segmented using these outlines, then (3) label brightness is calculated from edge-to-center of the drawn cells. **(F, G, H)** Localization at 26 hpf of the F-actin marker phalloidin (F), the muscle nuclei label anti-Rbfox1l (G), and MyHC antibody A4.1025 (H). Data is plotted as percent of total image brightness from edge to center of segments, with bootstrapped 95% confidence intervals in shaded lines. F-H uses the genotypic color code shown in (F). Inset in H shows the stark difference between MyHC localization in the *mylpfa*$^{+/-}$*;mylpfb*$^{+/-}$ double heterozygote and the *mylpfa*$^{-/-}$*;mylpfb*$^{-/-}$ double mutant, unobscured by other genotypes. Scalebar in A is for A-D; A' is for A'-D'.

Figure 7: The *mylpfa*$^{-/-}$ and the *mylpfa*$^{-/-}$;*mylpfb*$^{-/-}$ double mutant animals do not swim at high speed but increase the frequency of slower movements. **(A-C)** Escape response in wild-type or *mylpfa*$^{-/-}$ animals, showing images captured 1/60th of a second apart (A, B). Blue line shows maximal tail bend, quantified in (C). **(D-H)** Box plots of of behaviors in a 25-minute interval, imaged using DanioVision. Genotypic color code is shown in (D), with gene names simplified to '*a*' (*mylpfa*) or '*b*' (*mylpfb*). Behavioral analysis incudes the highest speed movement in the interval (D), the percent of time spent swimming swiftly (E), the average speed (F) the distance traveled (G), and the percent of time swimming at slow speed (H). **(I)** A logarithmic plot of the proportion of time that select genotypes swim at different speeds, with bootstrap confidence intervals shown for each genotype. **(J)** The same data is shown after normalization to wild-type behaviors, plotted on a linear scale. **(K, L)** Phalloidin label in the wild-type larva (K) or the *mylpfa*$^{-/-}$ mutant (L), annotated to show the boundary between slow-twitch and fast-twitch muscle fibers at 6 dpf. **(M)** Box plot shows that slow-twitch myofibril CSA is increased in the *mylpfa*$^{-/-}$ mutant and reduced in the mutant by expression of *the mylpfa:mylpfa-GFP* transgene. Data in (K-M) comes from the dataset examined in Figure 3H-M for other measures. Scalebar in A is for A-B, in K is for K-L. Significance is determined using Tukey-Kramer comparisons after one-way ANOVA, shown as n.s. of P>0.1, * P<0.01, ** P<0.01 and *** P<0.001 in these comparisons. For comparison between groups bounded by zero, we used non-parametric Steel-Dwas comparisons (~~~ P<0.001).

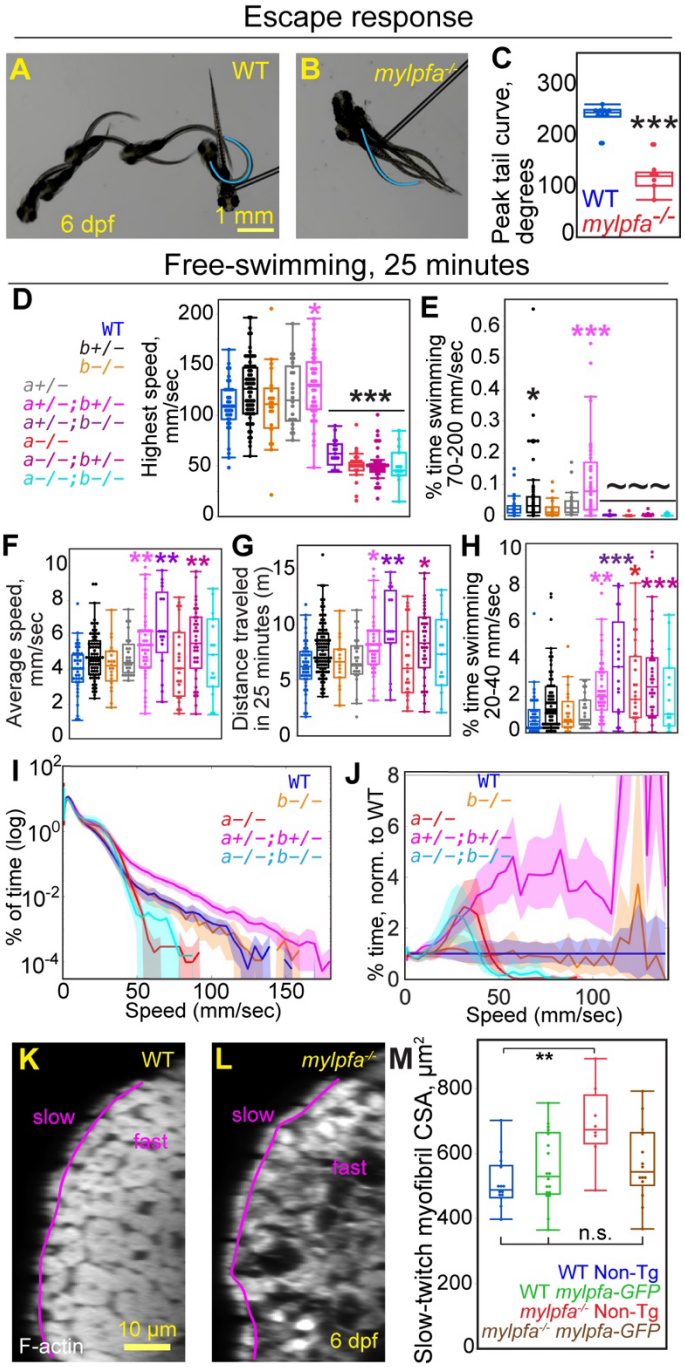

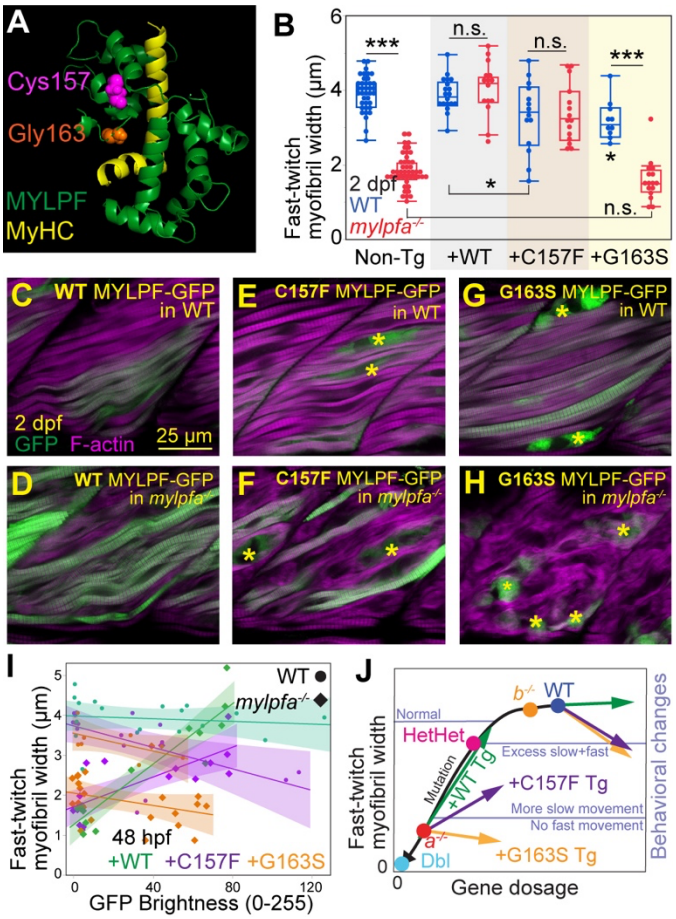

Figure 8: <u>*MYLPF* alleles modeling variants in Distal Arthrogryposis patients do not promote early myofibril assembly.</u> **(A)** Predicted MYLPF structure, with color and filled space highlighting the location of Cys157 and Gly163. **(B)** Box plots of myofibril widths in animals mosaic for the human MYLPF variants; the non-Tg group represents the compiled non-transgenic fibers from these animals. **(C-H)** Representative images of animals with mosaic expression of Mylpf transgenic variants (green), co-labeled for phalloidin (magenta) after fixation at 48 hpf. Animals are injected with the constructs *mylpfa:MYLPF-GFP,* expressing the WT MYLPF variant (C, D), C157F variant (E, F), and G163S variant(G, H). Areas with delocalized GFP are marked with an asterisk. **(I)** Scatterplot showing correlates between myofibril width and GFP brightness for all constructs injected. **(J)** Model of how gene dosage impacts myofibril formation and fish behaviors during zebrafish embryonic development. Significance determined by Tukey-Kramer HSD comparisons after ANOVA: n.s. is P>0.1, * indicates P<0.05, *** indicates P<0.001. Scalebar in C is for C-H.

Supplemental Figures and legends

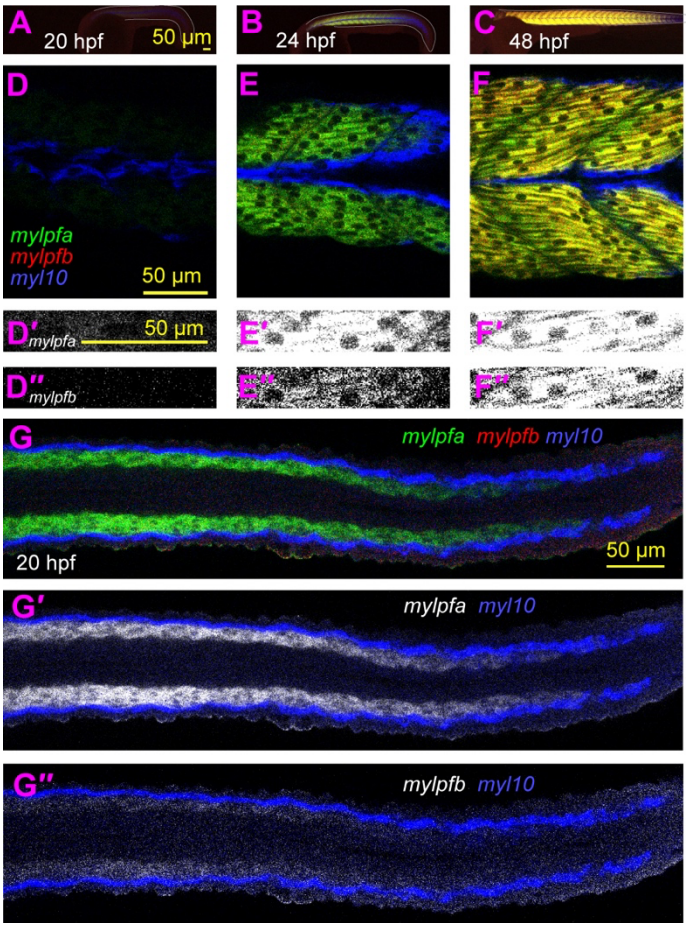

Figure S1: Time-course of *mylpfa* and *mylpfb* expression in fast-twitch muscle fibers. Images of HCR ISH for *mylpfa*, *mylpfb*, and the slow muscle marker *myl10.* **(A-C)** Low magnification images highlight that all three genes are expressed specifically in muscle and not in other body locations like the head. **(D-F″)** Confocal slices at higher magnification show that the two Mylpf genes are consistently excluded from slow-twitch fibers, but overlap in all fast-twitch fibers. Both genes are visible in the brightened single-channel inset at the stages examined (D′-F″). The ratio of *mylpfa* to *mylpfb* is somewhat lower in these co-labeled images (detected in 488 and 568 excitation) than in the single-channel ones shown in Figure 1G, H (detected in 488 channel), because of differential sensitivities between 488 and 568 detectors. **(G-G″)** Z-slice from a 20 hpf embryo shown from a transverse view, shown as a 3-color merge (G), merge of *myl10* and *mylpfa* (G**″**), and as a merge of *myl10* and *mylpfb* channels (G″). Both genes are present in fast-twitch myofibers, which are medial to slow twitch fibers by 20 hpf. Scalebar in A is for A-C, D is for D-F, D′ is for D′-F″, and G is for G-G″. Image settings are matched in A-C, D-F, and D′-F′ to allow comparisons between timepoints.

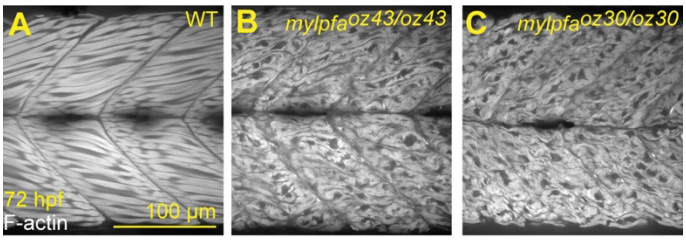

Figure S2: The *mylpfa*^{oz30} phenotypes are consistent with those found in the *mylpfa*^{oz43} mutant. **(A-C)** Confocal slices through the fast-twitch region of somites labeled for phalloidin at 72 hpf. Compared to wild-type siblings (A), myofibrils are disarrayed in the *mylpfa*^{oz30} mutant (B) and the *mylpfa*^{oz43} mutant (C). Scale bar in A applies to A-C.

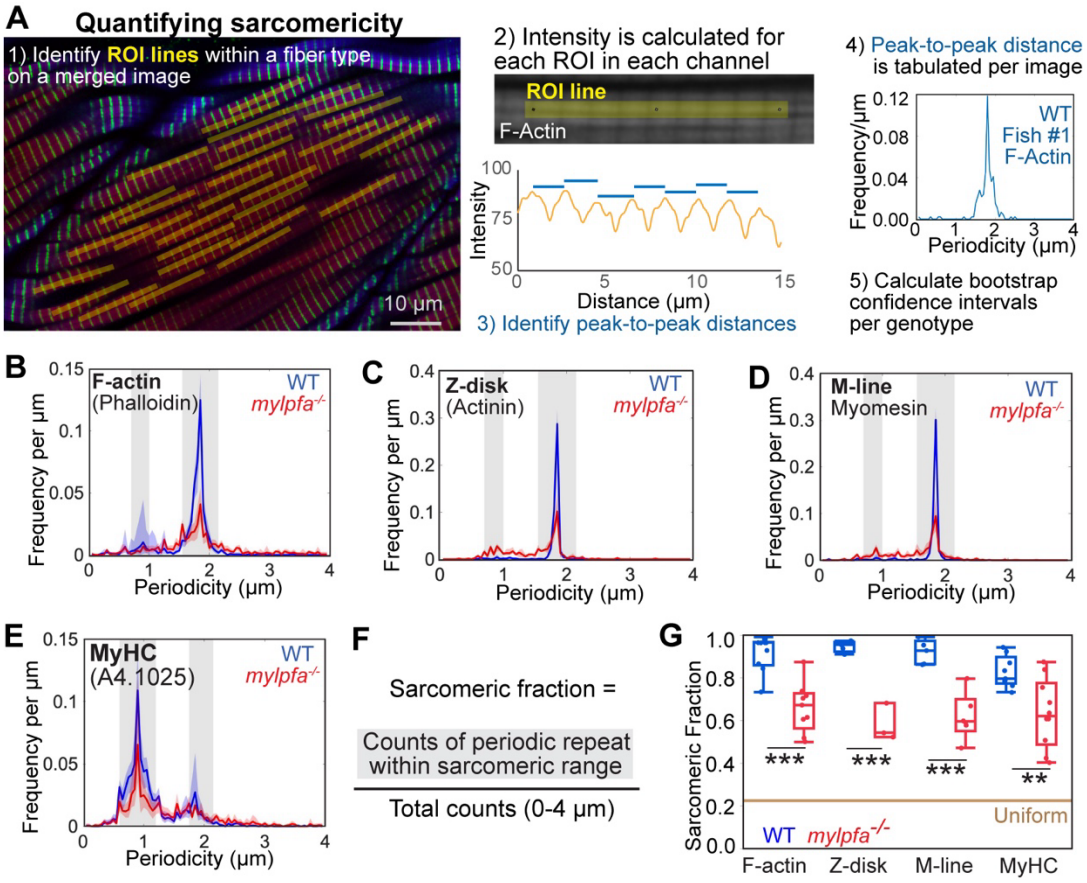

Figure S3: Explanation of the sarcomeric fraction calculation. **(A)** Overview of a method to quantify the degree to which markers localize to sarcomeres. 1) ROI lines are drawn throughout the fast-twitch muscle region of a dorsal somite half, with lengths of approximately 15 µm each. 2) An ImageJ script separates channels and calculates grayscale intensity across the ROI line shown on top of the F-actin channel. 3) The periodicity of each ROI is calculated, and repeats are binned by length. 4) Histogram plot of all ROI in one image, here binned to step size 0.05 µm, with peak frequency near the sarcomere length of 1.85 µm. 5) Each 0.05 µm histogram bin is averaged per image, then bootstrap confidence intervals are calculated using variation between images. **(B-E)** Histograms showing the frequency of periodicity in images. Colored lines represent mean values per genotype, semi-transparent colored lines indicate bootstrap confidence intervals, and gray bars indicating the sarcomeric intervals per marker. **(F)** Formula for calculating sarcomeric fraction, which is the ratio of signal in sarcomeric lengths (gray bars) to total localization (Y-axis, 0-4 µm) is the sarcomeric fraction. **(G)** Sarcomeric fractions are shown for F-actin (phalloidin), Z-disk (Actinin), M-line (Myomesin), and MyHC (A4.1025) labels. A horizontal brown line shows the fraction predicted by a uniform distribution. Data in S3B and S3G are replicated in main-text Figures 2K and 2L respectively. For all bar graphs and histogram plots, wild-type data is blue, and the *mylpfa*$^{-/-}$ mutant data is red. Significance thresholds were determined by Tukey-Kramer HSD comparisons; ** P<0.01, *** P<0.001.

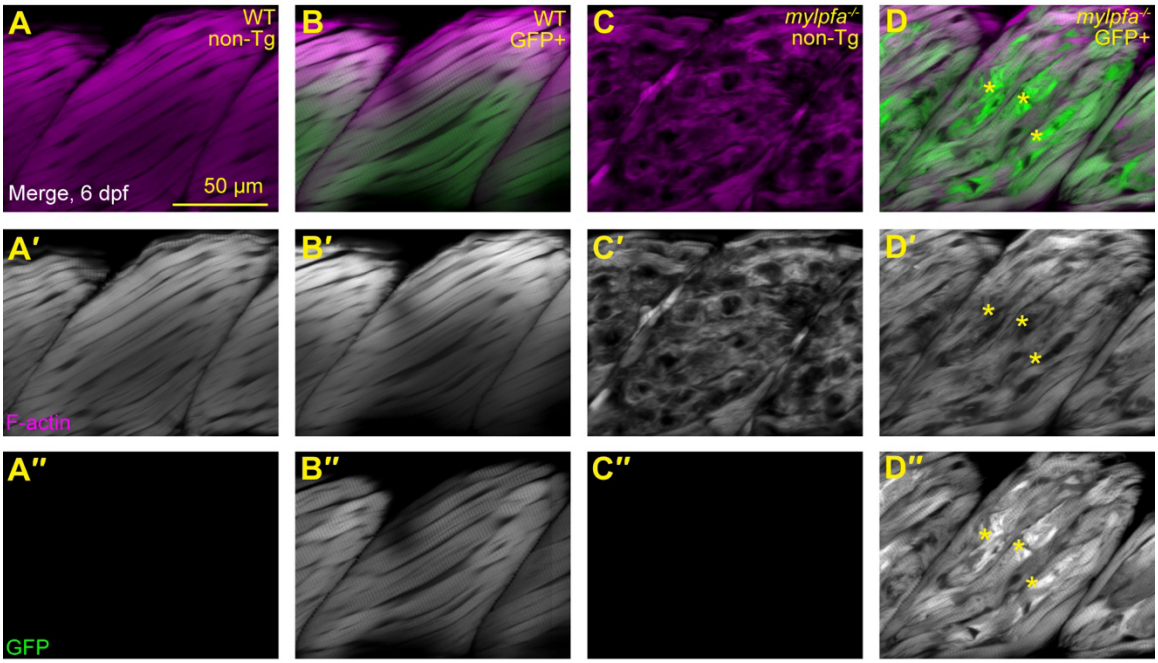

Figure S4: Representative examples of the *mylpfa-GFP* rescue experiments at 6 dpf. **(A-D″)** Confocal slices in sagittal view showing the dorsal half of somites. Images are shown as an overlay of phalloidin and GFP channels (A-D), as single channel for phalloidin (A′-D′), or as single channel for GFP (A″-D″),. At this stage we sometimes find patches of disordered GFP and Actin in the *mylpfa*$^{-/-}$ mutant at 6 dpf (asterisks) alongside the well-ordered myofibrils. Scalebar in A applies to all panels.

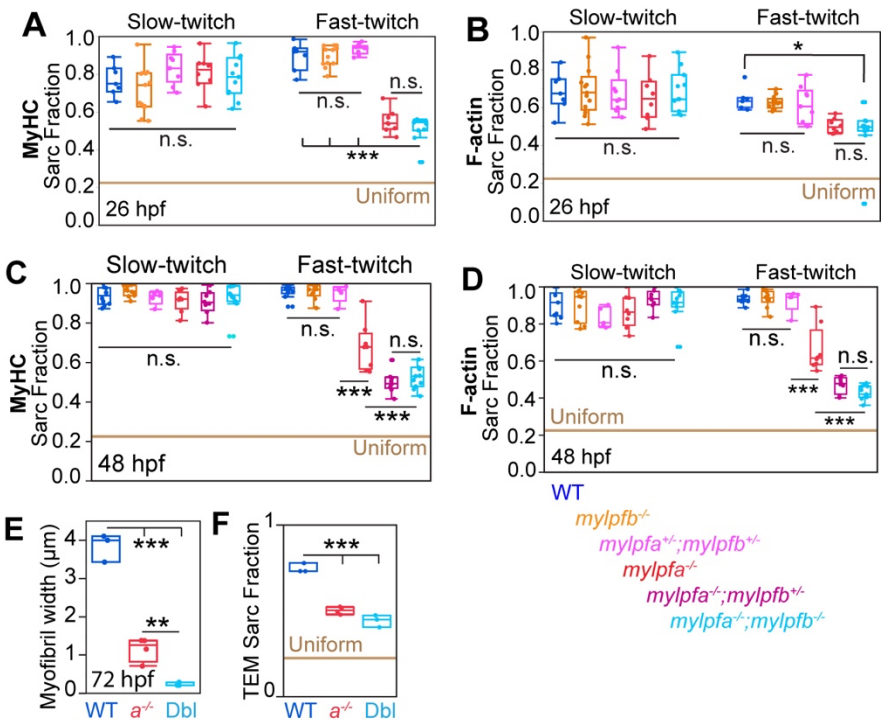

Figure S5: Comparison of muscle phenotypes in the *mylpfa*$^{-/-}$;*mylpfb*$^{-/-}$ incross through embryonic development. **(A)** Box plots showing the fraction of sarcomeric MyHC at 26hpf, **(B)** F-actin at 26 hpf, **(C)** MyHC at 48 hpf, and **(D)** F-actin at 48 hpf. Although F-actin localizes first, its periodicity increases later than MyHC so the shifts in the mutant are smaller for that gene in the earlier timepoint. The mutant's reduction in myofibril width and loss of sarcomeres persists to 72 hpf as seen in measurements of **(E)** myofibril width and **(F)** fraction of sarcomere-length objects in TEM. Genotypic color codes are shown in the figure. Significance thresholds were determined by Tukey-Kramer HSD comparisons (K); not significant (n.s.) is P>0.1, ** P<0.01, *** P<0.001.

Video 1: The *mylpfa*$^{-/-}$ mutant shows an impaired escape response. Imaging at 240 frames/second, showing 100 msec after contact with fishing line in the wild-type and the *mylpfa*$^{-/-}$ mutant. Both animals respond to the prodding; however, the *mylpfa*$^{-/-}$ mutant escapes at slower speed due to smaller tail undulations. Figure 7A, B shows a projection of frames from this video.

Tables:

n/a

Citations

1. Luis, N. M. & Schnorrer, F. Mechanobiology of muscle and myofibril morphogenesis. *Cells & Development* **168**, 203760 (2021).
2. Berger, J., Berger, S. & Currie, P. D. Mob4-dependent STRIPAK involves the chaperonin TRiC to coordinate myofibril and microtubule network growth. *PLoS Genet* **18**, e1010287 (2022).
3. Sanger, J. W. *et al.* Assembly and Maintenance of Myofibrils in Striated Muscle. in *The Actin Cytoskeleton* (ed. Jockusch, B. M.) vol. 235 39–75 (Springer International Publishing, Cham, 2016).
4. Holtzer, H. *et al.* Independent assembly of 1.6 microns long bipolar MHC filaments and I-Z-I bodies. *Cell Struct Funct* **22**, 83–93 (1997).
5. Rhee, D., Sanger, J. M. & Sanger, J. W. The premyofibril: Evidence for its role in myofibrillogenesis. *Cell Motility* **28**, 1–24 (1994).
6. Raeker, M. Ö., Shavit, J. A., Dowling, J. J., Michele, D. E. & Russell, M. W. Membrane-myofibril cross-talk in myofibrillogenesis and in muscular dystrophy pathogenesis: lessons from the zebrafish. *Frontiers in Physiology* **5**, (2014).
7. Weitkunat, M., Brasse, M., Bausch, A. R. & Schnorrer, F. Mechanical tension and spontaneous muscle twitching precede the formation of cross-striated muscle *in vivo*. *Development* **144**, 1261–1272 (2017).
8. Tskhovrebova, L. & Trinick, J. Titin and Nebulin in Thick and Thin Filament Length Regulation. in *Fibrous Proteins: Structures and Mechanisms* (eds. Parry, D. A. D. & Squire, J. M.) vol. 82 285–318 (Springer International Publishing, Cham, 2017).

1010 9. Loison, O. *et al.* Polarization-resolved microscopy reveals a muscle myosin motor-
1011 independent mechanism of molecular actin ordering during sarcomere maturation. *PLOS*
1012 *Biology* **16**, e2004718 (2018).
1013 10. Lemke, S. B. & Schnorrer, F. Mechanical forces during muscle development. *Mechanisms of*
1014 *Development* **144**, 92–101 (2017).
1015 11. Hall, T. E. *et al.* In vivo cell biological screening identifies an endocytic capture mechanism
1016 for T-tubule formation. *Nat Commun* **11**, 3711 (2020).
1017 12. Lowey, S. & Trybus, K. M. Role of Skeletal and Smooth Muscle Myosin Light Chains.
1018 *Biophysical Journal* **68**, 7 (1995).
1019 13. Heissler, S. M. & Sellers, J. R. Myosin light chains: Teaching old dogs new tricks.
1020 *BioArchitecture* **4**, 169–188 (2014).
1021 14. Sherwood, J. J., Waller, G. S., Warshaw, D. M. & Lowey, S. A point mutation in the
1022 regulatory light chain reduces the step size of skeletal muscle myosin. *Proceedings of the*
1023 *National Academy of Sciences* **101**, 10973–10978 (2004).
1024 15. VanBuren, P. *et al.* The essential light chain is required for full force production by skeletal
1025 muscle myosin. *Proceedings of the National Academy of Sciences* **91**, 12403–12407 (1994).
1026 16. Pastra-Landis, S. C. & Lowey, S. Myosin subunit interactions. Properties of the 19,000-dalton
1027 light chain-deficient myosin. *J. Biol. Chem.* **261**, 14811–14816 (1986).
1028 17. Warmke, J., Yamakawa, M., Molloy, J., Falkenthal, S. & Maughan, D. Myosin light chain-2
1029 mutation affects flight, wing beat frequency, and indirect flight muscle contraction kinetics
1030 in Drosophila. *The Journal of cell biology* **119**, 1523–1539 (1992).

1031 18. Ravenscroft, G. *et al.* Bi-allelic mutations in MYL1 cause a severe congenital myopathy.
1032 *Human Molecular Genetics* (2018) doi:10.1093/hmg/ddy320.
1033 19. Nawrotzki, R., Fischman, D. A. & Mikawa, T. Antisense suppression of skeletal muscle
1034 myosin light chain-1 biosynthesis impairs myofibrillogenesis in cultured myotubes. *J Muscle*
1035 *Res Cell Motil* **16**, 45–56 (1995).
1036 20. Lossie, J. *et al.* Mutations of ventricular essential myosin light chain disturb myosin binding
1037 and sarcomeric sorting. *Cardiovascular Research* **93**, 390–396 (2012).
1038 21. Cao, J. *et al.* The single-cell transcriptional landscape of mammalian organogenesis. *Nature*
1039 **566**, 496–502 (2019).
1040 22. Wang, Y. *et al.* Fast skeletal muscle regulatory light chain is required for fast and slow
1041 skeletal muscle development. *The FASEB Journal* **21**, 2205–2214 (2007).
1042 23. Hall, J. G. Arthrogryposis (multiple congenital contractures): Diagnostic approach to
1043 etiology, classification, genetics, and general principles. *European Journal of Medical*
1044 *Genetics* **57**, 464–472 (2014).
1045 24. Bamshad, M., Van Heest, A. E. & Pleasure, D. Arthrogryposis: A Review and Update: *The*
1046 *Journal of Bone and Joint Surgery-American Volume* **91**, 40–46 (2009).
1047 25. Whittle, J., Johnson, A., Dobbs, M. B. & Gurnett, C. A. Models of Distal Arthrogryposis and
1048 Lethal Congenital Contracture Syndrome. *Genes* **12**, 943 (2021).
1049 26. Devoto, S. H., Melançon, E., Eisen, J. S. & Westerfield, M. Identification of separate slow and
1050 fast muscle precursor cells in vivo, prior to somite formation. *Development* **122**, 3371–3380
1051 (1996).

1052 27. Mead, A. F., Kennedy, G. G., Palmer, B. M., Ebert, A. M. & Warshaw, D. M. Mechanical
1053 Characteristics of Ultrafast Zebrafish Larval Swimming Muscles. *Biophysical Journal* **119**,
1054 806–820 (2020).
1055 28. Talbot, J. & Maves, L. Skeletal muscle fiber type: using insights from muscle developmental
1056 biology to dissect targets for susceptibility and resistance to muscle disease. *Wiley*
1057 *Interdiscip Rev Dev Biol* **5**, 518–534 (2016).
1058 29. Roy, S. D. *et al.* Myotome adaptability confers developmental robustness to somitic
1059 myogenesis in response to fibre number alteration. *Developmental Biology* **431**, 321–335
1060 (2017).
1061 30. Farnsworth, D. R., Saunders, L. M. & Miller, A. C. A single-cell transcriptome atlas for
1062 zebrafish development. *Developmental Biology* **459**, 100–108 (2020).
1063 31. Sur, A. *et al.* Single-cell analysis of shared signatures and transcriptional diversity during
1064 zebrafish development. *Developmental Cell* S1534580723005774 (2023)
1065 doi:10.1016/j.devcel.2023.11.001.
1066 32. Thisse, B. *et al.* Spatial and temporal expression of the zebrafish genome by large-scale in
1067 situ hybridization screening. *Methods Cell Biol* **77**, 505–519 (2004).
1068 33. Xu, Y., He, J., Wang, X., Lim, T. M. & Gong, Z. Asynchronous activation of 10 muscle-specific
1069 protein (MSP) genes during zebrafish somitogenesis. *Developmental Dynamics* **219**, 201–
1070 215 (2000).
1071 34. Nassar, L. R. *et al.* The UCSC Genome Browser database: 2023 update. *Nucleic Acids Res* **51**,
1072 D1188–D1195 (2023).

1073 35. Chong, J. X. *et al.* Mutations in MYLPF Cause a Novel Segmental Amyoplasia that Manifests
1074 as Distal Arthrogryposis. *The American Journal of Human Genetics* **107**, 293–310 (2020).
1075 36. Ju, B. *et al.* Recapitulation of fast skeletal muscle development in zebrafish by transgenic
1076 expression of GFP under the mylz2 promoter. *Developmental Dynamics* **227**, 14–26 (2003).
1077 37. Jackson, H. E. *et al.* The role of Sox6 in zebrafish muscle fiber type specification. *Skeletal*
1078 *Muscle* **5**, 2 (2015).
1079 38. Gangras, P. *et al.* Zebrafish rbm8a and magoh mutants reveal EJC developmental functions
1080 and new 3'UTR intron-containing NMD targets. *PLoS Genet* **16**, e1008830 (2020).
1081 39. Roberts, J. A. *et al.* Targeted transgene integration overcomes variability of position effects
1082 in zebrafish. *Development* **141**, 715–724 (2014).
1083 40. Karuppasamy, M. *et al.* Standardization of zebrafish drug testing parameters for muscle
1084 diseases. *Disease Models & Mechanisms* **17**, dmm050339 (2024).
1085 41. Bernick, E. P., Zhang, P.-J. & Du, S. Knockdown and overexpression of Unc-45b result in
1086 defective myofibril organization in skeletal muscles of zebrafish embryos. *BMC Cell Biology*
1087 **11**, 70 (2010).
1088 42. Burghardt, T. P., Sun, X., Wang, Y. & Ajtai, K. In vitro and in vivo single myosin step-sizes in
1089 striated muscle. *Journal of Muscle Research and Cell Motility* **36**, 463–477 (2015).
1090 43. Zhao, S. *et al.* Myosin-18B Promotes Mechanosensitive CaMKK2-AMPK-VASP Regulation of
1091 Contractile Actin Stress Fibers. *iScience* **23**, (2020).
1092 44. Berger, J., Berger, S., Li, M. & Currie, P. D. Myo18b is essential for sarcomere assembly in
1093 fast skeletal muscle. *Human molecular genetics* **26**, 1146–1156 (2017).

1094 45. Gurung, R. *et al.* A Zebrafish Model for a Human Myopathy Associated with Mutation of the
1095 Unconventional Myosin MYO18B. *Genetics* **205**, 725–735 (2017).
1096 46. Okamoto, H. *et al.* Molecular characterization of mutant actin genes which induce heat-
1097 shock proteins in *Drosophila* flight muscles. *The EMBO Journal* **5**, 589–596 (1986).
1098 47. Whittle, J. *et al.* MYH3-associated distal arthrogryposis zebrafish model is normalized with
1099 para-aminoblebbistatin. *EMBO Mol Med* e12356 (2020) doi:10.15252/emmm.202012356.
1100 48. Zempo, B., Yamamoto, Y., Williams, T. & Ono, F. Synaptic silencing of fast muscle is
1101 compensated by rewired innervation of slow muscle. *Sci. Adv.* **6**, eaax8382 (2020).
1102 49. Naganawa, Y. & Hirata, H. Developmental transition of touch response from slow muscle-
1103 mediated coilings to fast muscle-mediated burst swimming in zebrafish. *Developmental*
1104 *Biology* **355**, 194–204 (2011).
1105 50. Lobjois, V. *et al.* A muscle transcriptome analysis identifies positional candidate genes for a
1106 complex trait in pig. *Animal Genetics* **39**, 147–162 (2008).
1107 51. Ryan, M. T. *et al.* Polymorphisms in the regulatory region of the porcine MYLPF gene are
1108 related to meat quality traits in the Large White breed. *Meat Science* **113**, 104–106 (2016).
1109 52. Zhang, R. *et al.* The Expression Profiles of mRNAs and lncRNAs in Buffalo Muscle Stem Cells
1110 Driving Myogenic Differentiation. *Frontiers in Genetics* **12**, (2021).
1111 53. Aoki, H., Sadoshima, J. & Izumo, S. Myosin light chain kinase mediates sarcomere
1112 organization during cardiac hypertrophy in vitro. *Nat Med* **6**, 183–188 (2000).
1113 54. Westerfield, M. *The Zebrafish Book: A Guide for the Laboratory Use of Zebrafish (Danio*
1114 *Rerio).* (University of Oregon Press, Eugene, 2007).

1115 55. Kimmel, C. B., Ballard, W. W., Kimmel, S. R., Ullmann, B. & Schilling, T. F. Stages of
1116 embryonic development of the zebrafish. *Developmental dynamics* **203**, 253–310 (1995).
1117 56. Talbot, J. C. & Amacher, S. L. A streamlined CRISPR pipeline to reliably generate zebrafish
1118 frameshifting alleles. *Zebrafish* **11**, 583–585 (2014).
1119 57. Kawakami, K. Transgenesis and Gene Trap Methods in Zebrafish by Using the Tol2
1120 Transposable Element. in *Methods in Cell Biology* vol. 77 201–222 (Academic Press, 2004).
1121 58. Ignatius, M. S. *et al.* In vivo imaging of tumor-propagating cells, regional tumor
1122 heterogeneity, and dynamic cell movements in embryonal rhabdomyosarcoma. *Cancer Cell*
1123 **21**, 680–693 (2012).
1124 59. Kwan, K. M. *et al.* The Tol2kit: a multisite gateway-based construction kit for Tol2
1125 transposon transgenesis constructs. *Dev Dyn* **236**, 3088–3099 (2007).
1126 60. Suster, M. L., Abe, G., Schouw, A. & Kawakami, K. Transposon-mediated BAC transgenesis in
1127 zebrafish. *Nature Protocols* **6**, 1998–2021 (2011).
1128 61. Bird, N. C., Windner, S. E. & Devoto, S. H. Immunocytochemistry to Study Myogenesis in
1129 Zebrafish. in *Myogenesis* (ed. DiMario, J. X.) vol. 798 153–169 (Humana Press, Totowa, NJ,
1130 2012).
1131 62. Talbot, J. C., Johnson, S. L. & Kimmel, C. B. hand2 and Dlx genes specify dorsal, intermediate
1132 and ventral domains within zebrafish pharyngeal arches. *Development* **137**, 2507–2517
1133 (2010).
1134 63. Berberoglu, M. A. *et al.* Satellite-like cells contribute to pax7 -dependent skeletal muscle
1135 repair in adult zebrafish. *Developmental Biology* **424**, 162–180 (2017).

1136 64. Grove, B. K. *et al.* A new 185,000-dalton skeletal muscle protein detected by monoclonal
1137 antibodies. *J Cell Biol* **98**, 518–524 (1984).
1138 65. Webster, C., Silberstein, L., Hays, A. P. & Blau, H. M. Fast muscle fibers are preferentially
1139 affected in Duchenne muscular dystrophy. *Cell* **52**, 503–513 (1988).
1140 66. Choi, H. M. T., Schwarzkopf, M. & Pierce, N. A. Multiplexed Quantitative In Situ
1141 Hybridization with Subcellular or Single-Molecule Resolution Within Whole-Mount
1142 Vertebrate Embryos: qHCR and dHCR Imaging (v3.0). in *In Situ Hybridization Protocols* (eds.
1143 Nielsen, B. S. & Jones, J.) 159–178 (Springer US, New York, NY, 2020). doi:10.1007/978-1-
1144 0716-0623-0_10.
1145 67. Gulbulak, U., Wellette-Hunsucker, A. G., Kampourakis, T. & Campbell, K. S. GelBox: Open-
1146 source software to improve rigor and reproducibility when analyzing gels and immunoblots.
1147 *American Journal of Physiology-Heart and Circulatory Physiology* (2024)
1148 doi:10.1152/ajpheart.00144.2024.
1149 68. Schindelin, J. *et al.* Fiji: an open-source platform for biological-image analysis. *Nat Methods*
1150 **9**, 676–682 (2012).
1151 69. Baek, M. *et al.* Accurate prediction of protein structures and interactions using a three-track
1152 neural network. *Science* **373**, 871–876 (2021).
1153 70. Mary, H. & Brouhard, G. J. *Kappa (κ): Analysis of Curvature in Biological Image Data Using*
1154 *B-Splines*. http://biorxiv.org/lookup/doi/10.1101/852772 (2019) doi:10.1101/852772.
1155